THIS MANUSCRIPT HAS BEEN SUBMITTED TO THE ANNALS OF GLACIOLOGY AND HAS NOT BEEN PEER-REVIEWED.

Emulator-based Bayesian calibration of a subglacial drainage model

Journal:	*Annals of Glaciology*
Manuscript ID	AOG-94-0488
Manuscript Type:	Article
Date Submitted by the Author:	24-Dec-2024
Complete List of Authors:	Hill, Tim; Simon Fraser University, Earth Sciences Flowers, Gwenn; Simon Fraser University, Earth Sciences Bingham, Derek; Simon Fraser University, Department of Statistics and Actuarial Science Hoffman, Matthew; Los Alamos National Laboratory, Fluid Dynamics and Solid Mechanics Group
Keywords:	Glacier hydrology, Ice-sheet modelling, Subglacial processes
Abstract:	Subglacial drainage models, often motivated by the relationship between hydrology and ice flow, sensitively depend on numerous unconstrained parameters. We explore using borehole water-pressure timeseries to calibrate the uncertain parameters of a popular subglacial drainage model, taking a Bayesian perspective to quantify the uncertainty in parameter estimates and in the calibrated model predictions. To reduce the computation time associated with Markov Chain Monte Carlo sampling, we construct a fast Gaussian process emulator to stand in for the subglacial drainage model. We first carry out a calibration experiment using synthetic observations consisting of model simulations with hidden parameter values as a demonstration of the method. Using real borehole water pressures measured in western Greenland, we find meaningful constraints on four of the eight model parameters and a factor-of-three reduction in uncertainty of the calibrated model predictions. These experiments illustrate Gaussian process-based Bayesian inference as a useful tool for calibration and uncertainty quantification of complex glaciological models using field data. However, significant differences between the calibrated model and the borehole data suggest that structural limitations of the model, rather than poorly constrained parameters or computational cost, remain the most important constraint on subglacial drainage modelling.

Annals of Glaciology 00(0) 0000 1

Emulator-based Bayesian calibration of a subglacial drainage model

Tim Hill[1], Gwenn E. Flowers[1], Derek Bingham[2], Matthew J. Hoffman[3]

[1] *Department of Earth Sciences, Simon Fraser University, Burnaby, BC, Canada*

[2] *Department of Statistics and Actuarial Science, Simon Fraser University, Burnaby, BC, Canada*

[3] *Fluid Dynamics and Solid Mechanics Group, Los Alamos National Laboratory, Los Alamos, NM, USA*

Correspondence: Tim Hill <tim_hill_2@sfu.ca>

ABSTRACT.

Subglacial drainage models, often motivated by the relationship between hydrology and ice flow, sensitively depend on numerous unconstrained parameters. We explore using borehole water-pressure timeseries to calibrate the uncertain parameters of a popular subglacial drainage model, taking a Bayesian perspective to quantify the uncertainty in parameter estimates and in the calibrated model predictions. To reduce the computation time associated with Markov Chain Monte Carlo sampling, we construct a fast Gaussian process emulator to stand in for the subglacial drainage model. We first carry out a calibration experiment using synthetic observations consisting of model simulations with hidden parameter values as a demonstration of the method. Using real borehole water pressures measured in western Greenland, we find meaningful constraints on four of the eight model parameters and a factor-of-three reduction in uncertainty of the calibrated model predictions. These experiments illustrate Gaussian process-based Bayesian inference as a useful tool for calibration and uncertainty quantification of complex glaciological models using field data. However, significant differences between the calibrated model and the borehole data suggest that structural limitations of the model, rather than poorly constrained parameters or computational cost, remain the most important constraint on subglacial drainage modelling.

1 INTRODUCTION

Subglacial drainage models have numerous uncertain parameters that control their behaviour (e.g., Werder and others, 2013; Hager and others, 2022). If accurate subglacial drainage models are important in reproducing realistic ice-flow patterns as is often claimed (e.g., Sommers and others, 2024; Khan and others, 2024), it follows that well-constrained model parameters are important for well-calibrated model predictions. Such predictions should have an associated uncertainty, and the predictive skill of any calibrated model should be critically assessed.

A common strategy used to select parameter values in a subglacial drainage model is to identify "low", "medium" and "high" values for a subset of influential parameters (e.g., Dow, 2022) and to sample these values with one-at-a-time (e.g., Khan and others, 2024) or, rarely, all-at-once (e.g., Hager and others, 2022) sampling. In the absence of field data, parameter values may be selected based on producing a modelled drainage system consistent with prior expectations of realistic subglacial drainage (i.e., water pressure near ice overburden, seasonal development of subglacial channels) (e.g., Werder and others, 2013). When data are available, models have been tuned based on consistency with radar specularity (e.g., Dow and others, 2020; Hager and others, 2022), altimetry-derived subglacial lake dynamics (e.g., Wearing and others, 2024), and mapped locations of eskers and other subglacial landforms (Hepburn and others, 2024). Coupled hydrology–ice-flow models have also been tuned to match observed surface velocities (e.g., Ehrenfeucht and others, 2023; Khan and others, 2024).

A suite of field data has been used in inverse models to infer more about subglacial drainage properties than revealed by manual tuning. Certain parameter values, such as the roughness of englacial conduits, have been inferred from tracer experiments (e.g., Werder and Funk, 2009) and water pressure (e.g., Pohle and others, 2022). However, given the expected discrepancy between modelled and observed subglacial drainage, the parameter values that describe the real system may not produce the best model–data fit. Inverse modelling approaches have constrained subglacial channel-network characteristics such as channel radius and hydraulic gradient based on dense passive seismic measurements (e.g., Nanni and others, 2021) or a combination of borehole water-pressure timeseries and tracer transit times (e.g., Irarrazaval and others, 2019, 2021). Based on a dense borehole array, Rada Giacaman and Schoof (2023) characterized a spectrum of seasonal water-pressure patterns.

Formal model calibration and uncertainty quantification (e.g., Kennedy and O'Hagan, 2001; Higdon and others, 2004), based on evaluating the misfit between model outputs and actual data over the entire space of plausible parameter values, provides a path forward for constraining the values of all influential model parameters and determining the corresponding best model predictions with associated uncertainty. Formal calibration of subglacial drainage model parameters has rarely been attempted. For instance, Irarrazaval and others (2019, 2021) inferred the posterior distributions of channel network characteristics and hydraulic transmissivity by using a simplified, steady-state forward hydrology model to enable Bayesian inference. In the coupled hydrology–dynamics setting, calibration has been carried out by comparing modelled annual average surface velocities to satellite-derived velocity (Brinkerhoff and others, 2021).

In a previous study (Hill and others, 2024a), we constructed a Gaussian process emulator (e.g., Higdon and others, 2008) of the Glacier Drainage System (GlaDS) subglacial drainage model (Werder and others, 2013) that accelerates modelling by three orders of magnitude. In this study, we combine the Gaussian process emulator with borehole observations from western Greenland (Meierbachtol and others, 2013; Wright and others, 2016) to explore the possibility of more directly constraining subglacial drainage model parameters. Using Bayesian inference (e.g, Higdon and others, 2004; Gelman and others, 2013), we infer distributions of the eight most-uncertain GlaDS model parameters along with the corresponding uncertainty in calibrated model outputs. We first carry out a calibration experiment using a synthetic, model-generated water-pressure timeseries. Then, using real borehole water-pressure data, we derive posterior parameter distributions and calibrated model predictions, and assess the remaining uncertainty and discrepancy in drainage-system characteristics including water pressure.

2 REAL AND SYNTHETIC WATER-PRESSURE TIMESERIES

The calibration experiments are carried out on a $\sim$13,000 km^2 catchment in the Kangerlussuaq sector of western Greenland that includes Isunnguata Sermia, Russell Glacier and Leverett Glacier basins (Fig. 1). This well-studied portion of the ice sheet has been used extensively for in-situ and modelling studies of Greenland hydrology (e.g., Bartholomew and others, 2011; Sole and others, 2013; Lindbäck and others, 2015; Harper and others, 2021; Derkacheva and others, 2021), including previous emulator-based subglacial drainage modelling (Brinkerhoff and others, 2021; Verjans and Robel, 2024). Importantly, this sector of west Greenland has a suite of borehole timeseries data, including basal water pressure, obtained along a transect from near the margin up to 46 km inland spanning 2010–2015 (see Table 1 from Wright and others, 2016).

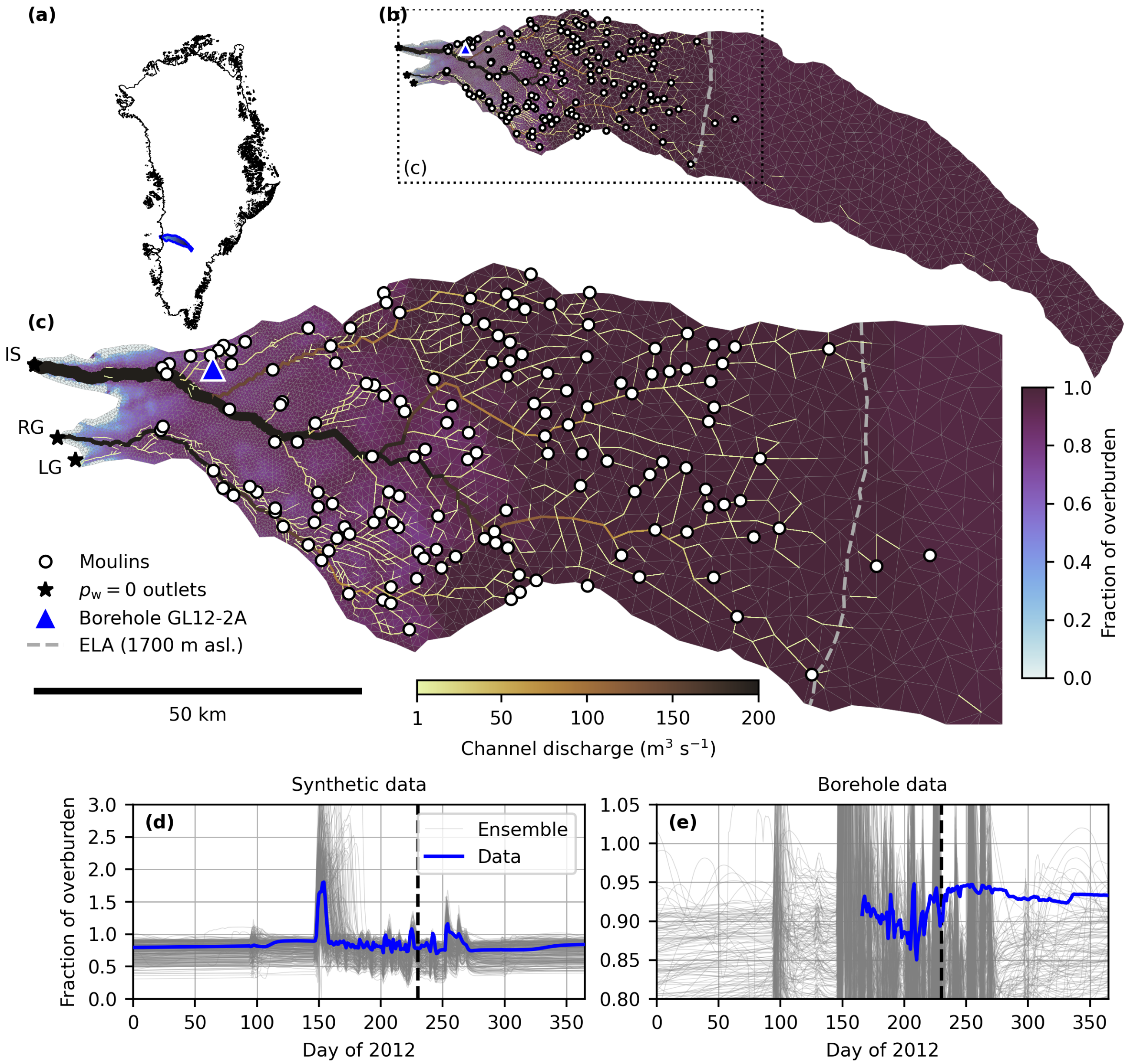

Fig. 1. Greenland numerical domain and calibration data. (a) Study area within Greenland Ice Sheet. (b) Flotation fraction and channel discharge for an example model output shown on numerical mesh, with moulin positions from Yang and Smith (2016), location of in-situ borehole water-pressure data (Meierbachtol and others, 2013; Wright and others, 2016) shown as a blue triangle, and approximate equilibrium line altitude sketched as dashed line (Smeets and others, 2018). (c) As in (b) but highlighting the area below 1850 m asl. with active moulins. Atmospheric pressure ($p_w = 0$) outlet nodes for Isunnguata Sermia (IS), Russel Glacier (RG) and Leverett Glacier (RG) are shown as black stars. (d) Ensemble of GlaDS-simulated flotation-fraction values and synthetic data. (e) Ensemble of GlaDS-simulated flotation-fraction values and in-situ borehole data (Meierbachtol and others, 2013; Wright and others, 2016). Vertical dashed line in (d, e) corresponds to the day shown in (b, c).

2.1 Borehole water-pressure data

We use hydraulic head measurements from a drilling campaign described in Meierbachtol and others (2013) and summarized by Wright and others (2016). Over the 2010–2015 period, a total of 32 boreholes were drilled to the bed, with 14 of these boreholes measuring basal water pressure. The majority of the boreholes where water pressure was measured were inferred to have intersected hydraulically isolated basal cavities (e.g., Meierbachtol and others, 2016). Since the subglacial drainage model is a continuum model that assumes hydraulically connected drainage across the domain, we select a single water-pressure timeseries from a borehole ∼27 km from the margin (67.204° N, 49.718° W; Fig. 1c), denoted GL12-2A, as the only timeseries representing hydraulically connected drainage and that includes data from within and outside of the melt season (Fig. 1e). This borehole intersects a bed trough approximately 3 km across and 200 m deep, where the ice thickness is 695.5 m as measured with the drilling hose (Wright and others, 2016). Hydraulic head values are converted into fraction of overburden using the reported ice thickness and assuming an ice density $\rho_{\mathrm{i}} = 910\,\mathrm{kg\,m^{-3}}$ (Wright and others, 2016). The flotation fraction timeseries spans 16 June 2012 to 24 July 2013, and we use the data from the beginning of the record only until the end of 2012 for calibration since the data quality degrades the longer the instruments are deployed (personal communication from J. Harper, 2024). We compute the daily mean of the ∼ 15-minute data for comparison with model outputs.

2.2 Synthetic water-pressure data

We carry out a synthetic calibration experiment on the domain described above as a methodological example and to derive an upper bound on the strength of constraints that could be learned from point-scale water-pressure timeseries. Since there will be irreducible discrepancy between the model output and real borehole data, the real calibration experiment is expected to produce weaker constraints. The synthetic water-pressure data consist of modelled water pressure (as described in Section 3) using hidden parameter values, and the goal of the experiment is to assess the accuracy and uncertainty in inferred values. We use outputs chosen from a simulation that has high winter water pressure and low summer water pressure relative to the median simulation,(Fig. 1d), since low winter water pressure is a common shortcoming of subglacial drainage models relative to observations (e.g., Downs and others, 2018).

3 FORWARD MODEL

3.1 Subglacial drainage model

We use the Glacier Drainage System (GlaDS) model (Werder and others, 2013) as the physically based forward model of subglacial drainage. GlaDS represents interacting distributed and channelized drainage systems. Distributed drainage is modelled as macroporous sheet flow and is intended to represent area-averaged flow through a network of hydraulically connected cavities formed in the lee of bed obstacles. Sheet flow transitions between laminar and turbulent regimes depending on the local Reynolds number (Hill and others, 2024c). Channelized drainage is modelled as a network of one-dimensional R-channels, numerically located on the edges of mesh elements. The model does not represent hydraulically isolated or weakly connected drainage (e.g., Murray and Clarke, 1995; Andrews and others, 2014), which has been shown to play an important role in relating borehole water-pressure timeseries to surface velocity observations (Hoffman and others, 2016). We have therefore selected the borehole water-pressure record (as described above) that appears to best represent hydraulically connected drainage.

GlaDS requires specification of several poorly constrained parameters. We consider eight parameters, $[k_\mathrm{s}, k_\mathrm{c}, h_\mathrm{b}, r_\mathrm{b}, A, l_\mathrm{c}, \omega, e_\mathrm{v}]$ (defined in Table 1), as the uncertain parameters to be calibrated. One could in principle consider the channel-flow exponents α_c and β_c as uncertain calibration parameters as well, however, we assume flow in R-channels is well-described by turbulent Darcy-Weisbach flow and keep these parameters fixed. Other model parameters are physical constants, so we consider this to be a comprehensive assessment of parametric uncertainty, conditioned on the turbulent-channel assumption.

3.2 Model domain and discretization

The model domain is defined as a subglacial hydraulic catchment for the three proglacial outlets identified in Fig. 1. These outlets correspond to the Isortoq River (for the Isunnguata Sermia sub-catchment) and two branches of the Sandflugtsdalen River (for the Russell Glacier and Leverett Glacier sub-catchments) (Fig. 1 from Lindbäck and others, 2015). The catchment boundaries are defined by assuming water pressure is equal to ice overburden, $p_\mathrm{w} = \rho_\mathrm{i} g H$, using 150 m-resolution IceBridge BedMachine Greenland (Morlighem and others, 2017; Morlighem and others, 2022) for surface elevation, bed elevation and the land–ice mask. The numerical domain consists of a triangular mesh with 4897 nodes that is refined to have edge lengths ∼500 m below 1000 m asl. and as large as 5000 m above 2000 m asl. (Fig. 1). For calibration and to

Table 1. Constants (top group), fixed model parameters for GlaDS simulations (middle group) and input parameters and ranges used for training the Gaussian process emulator and inference (bottom group). The basal velocity u_b and basal melt rate $\dot{m}_\mathrm{s}$ are fixed, spatially varying fields, with bracketed values indicating the minimum and maximum.

	Parameter	Value	Units
ρ_w	Density of water	1000	$\mathrm{kg\,m^{-3}}$
ρ_i	Density of ice	910	$\mathrm{kg\,m^{-3}}$
g	Gravitational acceleration	9.81	$\mathrm{m\,s^{-2}}$
L	Latent heat of fusion	3.34×10^{5}	$\mathrm{J\,kg^{-1}}$
c_w	Specific heat capacity of water	4.22×10^{3}	$\mathrm{J\,kg^{-1}}$
c_t	Pressure melting coefficient	-7.50×10^{-8}	$\mathrm{K\,Pa^{-1}}$
ν	Kinematic viscosity of water at 0°C	1.793×10^{-6}	$\mathrm{m^2\,s^{-1}}$
α_c	Channel-flow exponent	5/4	–
β_c	Channel-flow exponent	3/2	–
u_b	Basal speed	[0.11, 52]	$\mathrm{m\,a^{-1}}$
n	Ice-flow exponent	3	–
$\dot{m}_\mathrm{s}$	Basal melt rate	[0.0026, 0.043]	$\mathrm{m\,w.e.\,a^{-1}}$
k_s	Sheet conductivity	[0.001, 0.1]	$\mathrm{Pa\,s^{-1}}$
k_c	Channel conductivity	[0.1, 1.0]	$\mathrm{m^{3/2}\,s^{-1}}$
h_b	Bed bump height	[0.05, 1]	m
r_b	Bed bump aspect ratio	[10, 100]	–
A	Ice flow-law coefficient	$[10^{-24}, 10^{-22}]$	$\mathrm{Pa^{-3}\,s^{-1}}$
l_c	Width of sheet beneath channels	[1, 100]	m
ω	Laminar–turbulent transition parameter	[1/500, 1/5000]	–
e_v	Englacial void fraction	$[10^{-4}, 10^{-3}]$	–

generate synthetic data (Section 2.2), we extract modelled values at a single node near the borehole that was chosen to be most representative of observed conditions (Fig. S1, S2).

3.3 Melt and basal velocity forcing

We force GlaDS with daily surface melt and steady basal melt fields. Surface melt rates consist of daily mean 5.5 km-resolution RACMO2.3p2 (Noël and others, 2018) surface runoff outputs for 2010–2013. Meltwater is routed to the bed through 148 moulins previously mapped by Yang and Smith (2016), with meltwater instantaneously accumulated within sub-catchments defined as Voronoi diagrams centered on each moulin. Basal melt rates are prescribed as the sum of melt rates from time-invariant geothermal and frictional heat fluxes. The geothermal flux linearly varies between $27\,\mathrm{mW\,m^{-2}}$ at the margin and $49\,\mathrm{mW\,m^{-2}}$ at the ice divide based on borehole observations (Meierbachtol and others, 2015). The frictional heat flux from sliding is computed as $|u_\mathrm{b}\tau_\mathrm{b}|$ for basal velocity u_b and basal drag τ_b. We assume that basal velocity u_b, and therefore basal drag and frictional heat flux, are constant in time while acknowledging that substantial seasonal melt-forced velocity variations are observed in this region (e.g., van de Wal and others, 2008; Derkacheva and others, 2021). Basal drag is approximated as equal to the driving stress, $\tau_\mathrm{b} = \rho_i g H |\nabla z_\mathrm{s}|$, where z_s is the surface elevation. Basal velocity is estimated as a uniform fraction of MEaSUREs multi-year (1995–2015) average surface velocities (Joughin and others, 2016, 2018) by computing the ratio (0.33) that results in a maximum frictional-melt rate of $4\,\mathrm{cm\,w.e.\,a^{-1}}$ to match maximum frictional-melt rates derived from borehole data and satellite observations (Harper and others, 2021).

3.4 Boundary and initial conditions

No-flux subglacial drainage conditions are prescribed everywhere along the boundary, except at the three proglacial outlets where we prescribe zero water pressure. The outflow nodes are chosen as the nodes with locally minimum hydraulic potential, assuming water pressure equal to ice overburden, near the prescribed outlets used to define the hydraulic catchment (Fig. 1). We do not include an outflow node for the Point 660 catchment between the IS and RG catchments (Lindbäck and others, 2015) since we do not find a clear hydraulic potential minimum in this location. The model is initialized with no channels, water pressure equal to ice overburden and water layer thickness equal to 20% of the bed bump height. We run the model from 2010 until the end of 2012 and discard the first two years (2010–2011) as a spin-up period to bring the model into a quasi-periodic state.

3.5 Numerics

For the large ensemble of GlaDS simulations (Section 4.3), we have found that it is necessary to use a 0.2 h timestep and a solver residual tolerance of 10^{-5}. This timestep is short compared to the daily melt-forcing frequency, and the 10^{-5} solver tolerance is smaller than often used for more typical GlaDS simulations. Using numerical parameters that are less strict results in noticeable changes in modelled water pressure for certain simulations in the ensemble (Fig. S16). Since we are purposely running GlaDs with unusual parameter values as part of the large ensemble, it is not unexpected that we need to be cautious in selecting numerical parameters to ensure that model runs are appropriately converged. We have also found that using simulations with numerical artifacts results in an emulator with high prediction error and parameter estimates that are inconsistent with the true parameter values in the synthetic calibration experiment since the simulation outputs do not change predictably with respect to model parameters.

4 INVERSE MODEL

4.1 Bayesian inference

Given timeseries observations of subglacial water pressure, we aim to estimate the GlaDS parameter values that produce modelled water pressure consistent with the observations. Let $\boldsymbol{y} \in \mathbb{R}^{n_t}$ be the standardized observations, consisting of a number n_t days of flotation fraction values. The observations $\boldsymbol{y}$ are standardized by subtracting the mean and dividing by the standard deviation of the simulation ensemble (Section 4.3). Consistent with previous work (e.g., Brinkerhoff and others, 2021), we apply a log-transform to the model parameters and standardize the log-parameters such that they fall in the interval $[0, 1]$. We denote the vector of log-standardized GlaDS parameters $\boldsymbol{t} \in [0, 1]^d$, where $d = 8$ is the number of calibration model parameters. With $F(\boldsymbol{t})$ the standardized (i.e., centred and scaled by the simulation mean and standard deviation) forward model (GlaDS) evaluated for log-standardized parameter values $\boldsymbol{t}$, we model the observations as being generated from the forward model evaluated for some unknown calibration parameter values $\boldsymbol{t} = \boldsymbol{\theta}$,

$$\boldsymbol{y} = F(\boldsymbol{\theta}) + \boldsymbol{\epsilon}_y. \tag{1}$$

The observation error $\boldsymbol{\epsilon}_y \sim \mathcal{N}(\mathbf{0}, \boldsymbol{\Sigma}_y)$ is modelled as multivariate normal with zero mean and covariance $\boldsymbol{\Sigma}_y = \lambda_y^{-1}\mathbf{I}$ parameterized by precision λ_y. That is, we assume that the observations $\boldsymbol{y}$ are multivariate normally distributed with mean given by the standardized forward model evaluated for the unknown calibration parameters $F(\boldsymbol{\theta})$ and with covariance $\boldsymbol{\Sigma}_y$: $\boldsymbol{y} \sim \mathcal{N}(F(\boldsymbol{\theta}), \boldsymbol{\Sigma}_y)$.

From Bayes' theorem, the distribution of the model parameters $\boldsymbol{\theta}$ given the data, also called the posterior distribution, is

$$P(\boldsymbol{\theta}|\boldsymbol{y}) \propto P(\boldsymbol{y}|\boldsymbol{\theta})P(\boldsymbol{\theta}). \tag{2}$$

The first term on the right-hand-side, $P(\boldsymbol{y}|\boldsymbol{\theta})$, called the likelihood, is the probability of sampling the data $\boldsymbol{y}$ from the model (1) given certain GlaDS parameters $\boldsymbol{\theta}$. The second term, $P(\boldsymbol{\theta})$, called the prior distribution, specifies our prior belief about the value of $\boldsymbol{\theta}$. Eq. (2) indicates that we should update our belief in the calibration parameter values $\boldsymbol{\theta}$ in light of the data $\boldsymbol{y}$. As is common for Bayesian inference (e.g., Higdon and others, 2004; Gelman and others, 2013), we approximate the posterior distribution by iteratively sampling from the posterior distribution with Metropolis-Hastings Markov Chain Monte Carlo (MCMC). However, each likelihood evaluation $P(\boldsymbol{y}|\boldsymbol{\theta})$ involves running a forward GlaDS simulation. For the GlaDS model as used here, which takes ~9 h to run, sampling from the posterior (Eq. 2) is intractable since the Metropolis-Hastings algorithm often require thousands of sequential iterations to approximate the posterior distribution. To avoid this complication, we construct an emulator to stand in for GlaDS (e.g., Higdon and others, 2004; Brinkerhoff and others, 2021).

4.2 Gaussian process emulator

Based on an ensemble of simulations with the forward model (GlaDS), the emulator estimates the simulated values for untested parameter values. We use a Gaussian process (GP) emulator that is more fully described by Hill and others (2024a). Instead of emulating the full spatiotemporal model outputs, here we emulate the flotation-fraction timeseries for the node representing the borehole. The GP requires additional parameters, which we call "hyperparameters", whose values must be estimated. We denote their calibration values $\boldsymbol{\phi}$ to distinguish them from parameters of the subglacial drainage model (Table 1). Fig. 2 summarizes the emulator-based calibration workflow.

Since GPs do not naturally scale to multivariate outputs such as a timeseries, we follow Higdon and others (2008) in simplifying the problem using a principal component basis representation for the forward model outputs. Letting p denote the number of principal component basis vectors used in the representa-

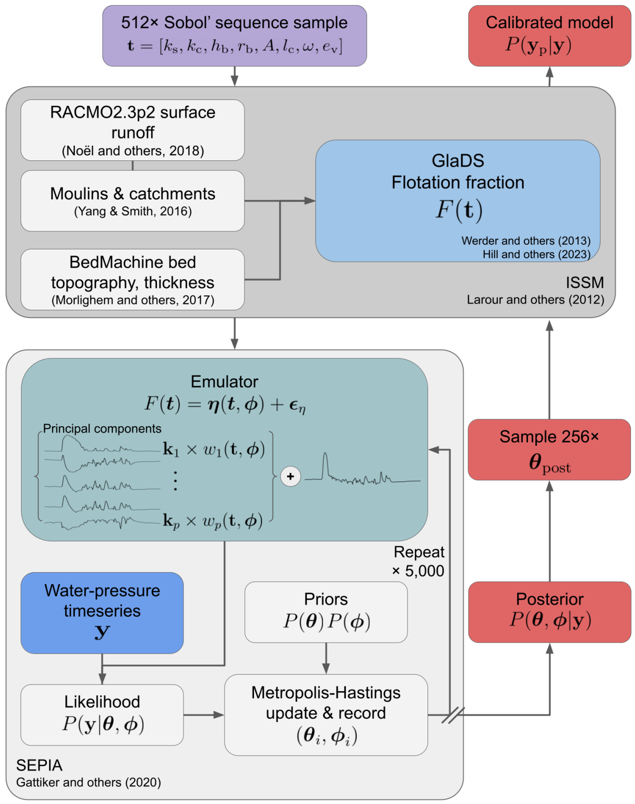

Fig. 2. Workflow for Gaussian process emulator-based calibration. $\boldsymbol{t}$ is the vector of log-standardized model parameters, with $\boldsymbol{t} = \boldsymbol{\theta}$ the calibration parameters that best fit the data $\boldsymbol{y}$, and $F(\boldsymbol{t})$ is the modelled timeseries of water pressure (expressed here as flotation fraction) corresponding to log-parameters $\boldsymbol{t}$. The emulator $\boldsymbol{\eta}$, with hyperparameters $\boldsymbol{\phi}$, is constructed as a linear combination of p principal component basis vectors $\boldsymbol{k}_j$ and independent scalar emulators w_j for $j = 1, \ldots, p$. Uncertainty in the calibrated model is estimated by Monte Carlo sampling from the posterior parameter distribution.

tion, we model the standardized forward model output as

$$F(\boldsymbol{t}) = \sum_{j=1}^{p} \boldsymbol{k}_j w_j(\boldsymbol{t}, \boldsymbol{\phi}) + \boldsymbol{\epsilon}_\eta, \tag{3}$$

where $\boldsymbol{k}_j$ $(1 \leq j \leq p)$ are the principal component basis vectors and w_j $(1 \leq j \leq p)$ are independent GPs. For convenience, we refer to the first term as the emulator $\eta(\boldsymbol{t}, \boldsymbol{\phi}) = \sum_{j=1}^{p} \boldsymbol{k}_j w_j(\boldsymbol{t}, \boldsymbol{\phi})$. The error term $\boldsymbol{\epsilon}_\eta \sim \mathcal{N}(\mathbf{0}, \lambda_\eta^{-1}\mathbf{I})$, represents basis truncation error and is parameterized by the emulator precision λ_η. The number of principal components p that are retained is an important choice as it influences the fidelity of the emulator predictions. We will select the number of principal components for each application by considering the proportion of variance in the simulation ensemble that is explained, the truncation error and by inspecting the residuals in the basis representation. Full details of the consequences of the basis representation, including an expression for the likelihood $P(\boldsymbol{y}|\boldsymbol{\theta}, \boldsymbol{\phi})$, are presented by Higdon and others (2008).

Each individual GP w_j is specified by its mean and covariance model. We use zero-mean GPs with a squared-exponential covariance function,

$$k_j(\boldsymbol{t}, \boldsymbol{t}') = \frac{1}{\lambda_{w,j}} \exp\left(-\sum_{i=1}^{d} \beta_{ij}(t_i - t_i')^2\right), \tag{4}$$

where $\lambda_{w,j}$ is the marginal precision (inverse variance) of the GP w_j and the β_{ij} $(i = 1, \ldots, d)$ hyperparameters control the strength of dependence on each of the inputs. In practice, a small additional diagonal covariance matrix parameterized by precision λ_n $(\mathcal{O}(10^3))$, sometimes called a nugget, is added to each GP covariance matrix to improve the numerical conditioning of the matrix. The complete hyperparameter vector, accounting for the p separate values for the GP marginal precision $\boldsymbol{\lambda}_w$, input sensitivity $\boldsymbol{\beta}$ and nugget $\boldsymbol{\lambda}_n$, is $\boldsymbol{\phi} = [\lambda_y, \lambda_\eta, \boldsymbol{\lambda}_w, \boldsymbol{\beta}, \boldsymbol{\lambda}_n]$.

We sample from the joint posterior distribution,

$$P(\boldsymbol{\theta}, \boldsymbol{\phi}|\boldsymbol{y}) \propto P(\boldsymbol{y}|\boldsymbol{\theta}, \boldsymbol{\phi})P(\boldsymbol{\theta})P(\boldsymbol{\phi}), \tag{5}$$

which accounts for the uncertainty in the data $\boldsymbol{y}$ (Eq. 1) as well as the replacement of the forward model with the GP emulator. We use the SEPIA package (Gattiker and others, 2020) v1.1 to construct the emulators and carry out Metrpolis-Hastings sampling. Choices for the prior distributions are discussed in

Table 2. Prior distributions on log-standardized subglacial drainage model parameters and Gaussian process hyperparameters. Uniform distributions $U(a,b)$ are parameterized by the interval $[a,b]$. Gamma distributions $\Gamma(a,b)$ are parameterized by the shape parameter a and the rate parameter b such that the mean is $\frac{a}{b}$.

	Parameter	Distribution
$\boldsymbol{\theta}$	Standardized GlaDS parameters	$U(0,1)$
λ_y	Observation precision	$\Gamma(5,5)$
λ_η	Simulation precision	$\Gamma(a_\eta, b_\eta)$
$\boldsymbol{\lambda}_w$	Gaussian process precision	$\Gamma(5,5)$
$\boldsymbol{\beta}$	Gaussian process input sensitivity	$\Gamma(5,5)$
$\boldsymbol{\lambda}_n$	Gaussian process nugget precision	$\Gamma(3,0.003)$

Section 4.3. The foundation in uncertainty quantification is a primary benefit of GP modelling compared to other deterministic options for the emulator. In particular, the addition of the emulator uncertainty to the observation uncertainty in defining the GP likelihood (Higdon and others, 2008) means that uncertainty in GP predictions is accounted for in inferring distributions of the model parameters. If the emulator has large uncertainty relative to the observational uncertainty, then the resulting posterior parameter distributions will be noticeably wider than had we used the forward model directly (e.g., Downs and others, 2023).

4.3 Ensemble design

We design the simulation ensemble to uniformly sample the log-standardized input space in order to construct an emulator with prediction performance that is approximately uniform across the log-inputs. For this, we use a Sobol' sequence (Sobol', 1967) over the logarithm of the parameters within the bounds provided in Table 1. We draw 512 samples from the Sobol' sequence, using its sequential design properties to evaluate emulator performance with power-of-2 subsets of the full sequence. We construct an independent set of inputs for testing the emulator consisting of 100 samples from a space-filling Latin hypercube design.

For parameters with a physical interpretation (e.g., the bed geometry as described by the bump height h_b and aspect ratio r_b, the ice-flow coefficient A and the laminar–turbulent transition parameter ω), we have chosen parameter ranges that encompass plausible values. For the remaining parameters, we have chosen their ranges to be reasonably wide while minimizing the number of unrealistic simulations, for example as indicated by water pressure exceeding 300% of overburden. We have found that this pressure constraint limits the lower bound of channel conductivity k_c, sheet conductivity k_s and englacial storage parameter e_v.

These ranges largely encompass the values commonly used for modelling Greenland outlet glaciers with the GlaDS model (e.g., Gagliardini and Werder, 2018; Cook and others, 2020; Ehrenfeucht and others, 2023; Hill and others, 2024c; Verjans and Robel, 2024; Khan and others, 2024). Some exceptions include literature values of the englacial storage parameter as low as $e_\mathrm{v} = 10^{-5}$ (e.g., Ehrenfeucht and others, 2023; Khan and others, 2024), channel conductivity as low as $k_\mathrm{c} = 0.05\,\mathrm{m}^{3/2}\,\mathrm{s}^{-1}$ (e.g., Khan and others, 2024), and an ice-flow coefficient $A = 2.5 \times 10^{-25}\,\mathrm{Pa}^{-3}\mathrm{s}^{-1}$ indicative of basal ice below the pressure-melting point (Ehrenfeucht and others, 2023). Considering the laminar–turbulent sheet-flow model, it is difficult to compare the sheet conductivity range except to studies using a laminar sheet-flow model. Gagliardini and Werder (2018) and Cook and others (2020) use a lower sheet conductivity value $k_\mathrm{s} \approx 2 \times 10^{-4}\,\mathrm{Pa\,s}^{-1}$, which we have found results in peak water pressures exceeding 300% of overburden for our setup.

4.4 Prior distributions

The prior distributions of GlaDS parameters $P(\boldsymbol{\theta})$ and GP hyperparameters $P(\boldsymbol{\phi})$ in (5) are used to express our belief in the values of these quantities. For model parameters $\boldsymbol{\theta}$, we take a uniform $U(0, 1)$ prior distribution for the log-standardized values to express a lack of prior belief of the most likely parameter values. We use Gamma distributions $\Gamma(a, b)$, parameterized by shape parameter a and rate parameter b, for the hyperparameter prior distributions $P(\boldsymbol{\phi})$ (Table 2) due to the flexibility of the Γ family of distributions and the fact that the probability density goes to 0 when $\boldsymbol{\phi} = 0$. Since the inputs are scaled to the range $\boldsymbol{t} \in [0, 1]^d$ and the outputs are centred and scaled to have unit variance, we select prior distributions for the observation precision λ_y, GP precision $\boldsymbol{\lambda}_\eta$ and GP sensitivity $\boldsymbol{\beta}$ that encourage values near 1. The GP nugget $\boldsymbol{\lambda}_n$ prior distribution encourages high precision (i.e., a small nugget) with a mean of 1000 and 95% interval spanning approximately an order of magnitude. We choose the prior distribution for the simulation precision λ_η to express our belief that this term should account for error in the truncated principal component basis. We choose the hyperparameters $a = a_\eta$ and $b = b_\eta$ to express this belief by constraining the mode to be equal to the precision of the basis representation, denoted λ_p. We have found that prescribing a prior distribution that allows a wide range of simulation-precision values can sometimes result in the simulation error term ϵ_η absorbing all of the variations in the output with respect to $\boldsymbol{\theta}$, leaving the GP to revert to the mean irrespective of the given values of $\boldsymbol{\theta}$. To express our belief that the GP should take up variations in the simulator response for different parameter values, and therefore that λ_η

represents the basis truncation error, we place 95% of the probability mass of the simulation-precision prior distribution within an interval with width equal to half of the basis precision λ_{p}. For the truncation error in synthetic and borehole calibration experiments, the prior distribution parameter values are approximately $a_\eta \approx 100$ and $b_\eta \approx 2$.

4.5 Posterior predictions

We produce calibrated GlaDS predictions by drawing 256 samples from the MCMC chain of GlaDS parameters (labelled $\boldsymbol{\theta}_{\mathrm{post}}$ in Fig. 2) and running the forward model (GlaDS) on the samples. Using GlaDS instead of the emulator to produce calibrated predictions allows us to investigate additional outputs such as the full spatiotemporal flotation fraction field and the distribution and extent of subglacial channels that are not predicted by the emulator.

5 RESULTS

5.1 Emulator performance

The root-mean-square error (RMSE) of the emulator flotation fraction predictions measured on the set of test simulations is relatively consistent for different choices of the number of principal components and the number of simulations in the ensemble used to train the emulator (Fig. S4), with median RMSE between 0.064–0.088 (in units of fraction of overburden). The RMSE decreases when increasing the number of principal components from 5 to 10, with minimal change for models with more principal components. Emulator performance improves for larger training ensembles, but with differences in the median performance remaining within the interquartile range. In other words, GP performance can be slightly improved by including more training simulations and principal components, but the error reduction is small compared to the variation in emulator error across the test set. The relatively weak sensitivity to the number of principal components and training simulations reported here is consistent with the more in-depth analysis carried out by Hill and others (2024a) for a simpler synthetic application. We choose to use the full set of 512 training simulations and 15 principal components, based on the levelling off of the emulator RMSE and the principal component truncation error (Fig. S3). In this case, the first 15 principal components explain 98% of the variation of the 512-member simulation ensemble.

The accuracy of the chosen emulator varies throughout the year and across the test set (Fig. 3). Emulator prediction error is highest in the spring (days ∼150–175) and for simulations with high peak

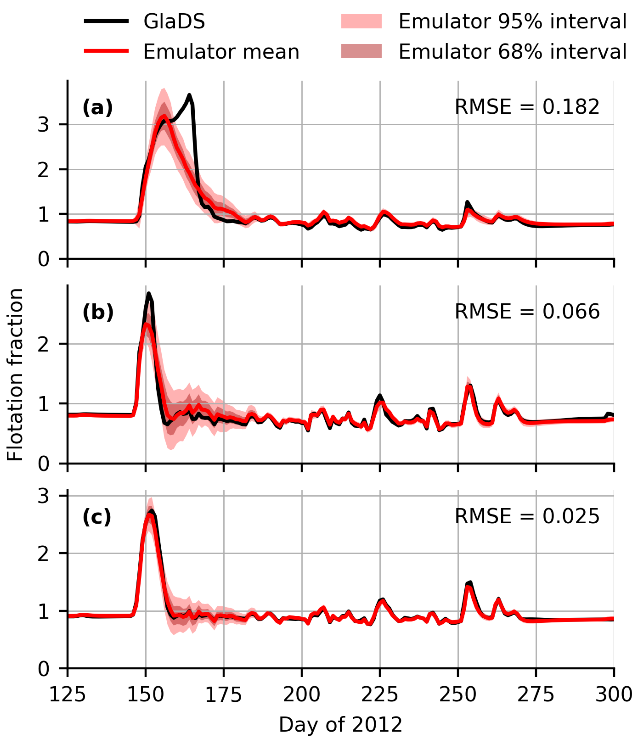

Fig. 3. Evaluation of the Gaussian process emulator. Comparison of GlaDS simulations and emulator predictions on the test set for individual simulations with high (95th-percentile, a), median (median, b) and low (5th-percentile, c) root-mean-square-error (RMSE).

water pressure (e.g., Fig. 3a). After day ~175, emulator predictions capture the amplitude and duration of water-pressure variations. Winter water pressure is reproduced within a few percent of overburden. Correspondingly, emulator predictions are most uncertain, as measured by the width of the 68% and 95% prediction intervals, between days 150–175, with uncertainty reducing to a small fraction of overburden by winter. The 95% emulator prediction intervals mostly overlap the simulated values, except in spring in Fig. 3a, indicating the emulator is appropriately estimating prediction uncertainty.

5.2 Synthetic calibration experiment

For the synthetic calibration experiment, which aims to recover the true but hidden parameter values used for a reference GlaDS simulation tht is labelled as data, emulator-based inference recovers the true parameter values within one standard deviation of the posterior distributions except for the sheet-channel width parameter l_c (Fig. 4, S13). For all parameters except the laminar–turbulent transition parameter ω, the marginal posterior distributions (diagonal panels in Fig. 4) are more informative than the prior distributions. The posterior estimates of the channel conductivity k_c, ice-flow coefficient A and the englacial storage parameter e_v are especially well-constrained relative to their prior distributions. We have found moderate pairwise correlations, including $r = 0.48$ between sheet conductivity k_s and the bed bump aspect ratio h_b, and $r = 0.48$ between channel conductivity k_c and the ice-flow coefficient A. The relatively weaker constraints on remaining parameters, including the lack of constraint on ω, are consistent with a previous analysis of the sensitivity of flotation fraction to these parameters (Hill and others, 2024a).

Repeating the calibration experiment by individually considering each of the 100 test simulations as data, we have found these calibration results to be robust with respect to the simulation that is chosen to be labelled as data. We consistently infer strong constraints on the the value of the channel conductivity k_c, ice-flow coefficient A, englacial storage parameter e_v and the bed bump aspect ratio r_b (Fig. S14) with very little bias (Fig. S15). While we typically constrain the sheet conductivity k_s, bed bump height b and sheet-channel width l_c values relative to their prior distributions, the true values are more likely to be in a lower posterior probability region (Table S1).

Calibrated model predictions have a 95% prediction interval that is 3.8 times narrower than that of the ensemble of simulations with parameter values sampled from the uniform priors (Fig. 5). As expected with synthetic data produced by the model, the calibrated predictions always overlap the synthetic data within the 95% prediction interval and often within the 68% interval (i.e., approximately within one standard deviation of the mean). While flotation fraction values between days $\sim$150–200 have been constrained relative to the prior distribution, there remains a spread of $\sim$100% of overburden in the 95% prediction intervals. However, this has been reduced from a spread of >200% of overburden in the original ensemble. The main discrepancy between the calibrated mean and the synthetic data is during the late-season melt events near day 250. Perhaps as a result of the biased posterior modes, the calibrated model has a faster flotation-fraction decay between these melt events than in the synthetic data.

5.3 Borehole calibration experiment

For the borehole data that covers the last 199 days (16 June to 31 December) of 2012, we choose to emulate only the corresponding period of modelled water pressure, rather than modelling the entire year as was done in the synthetic calibration experiment. This simplification allows us to reduce the number of principal components used by the emulator from 15 to 12 while still explaining 98% of the variance of the ensemble. We continue to use the full ensemble of 512 simulations to train the emulator.

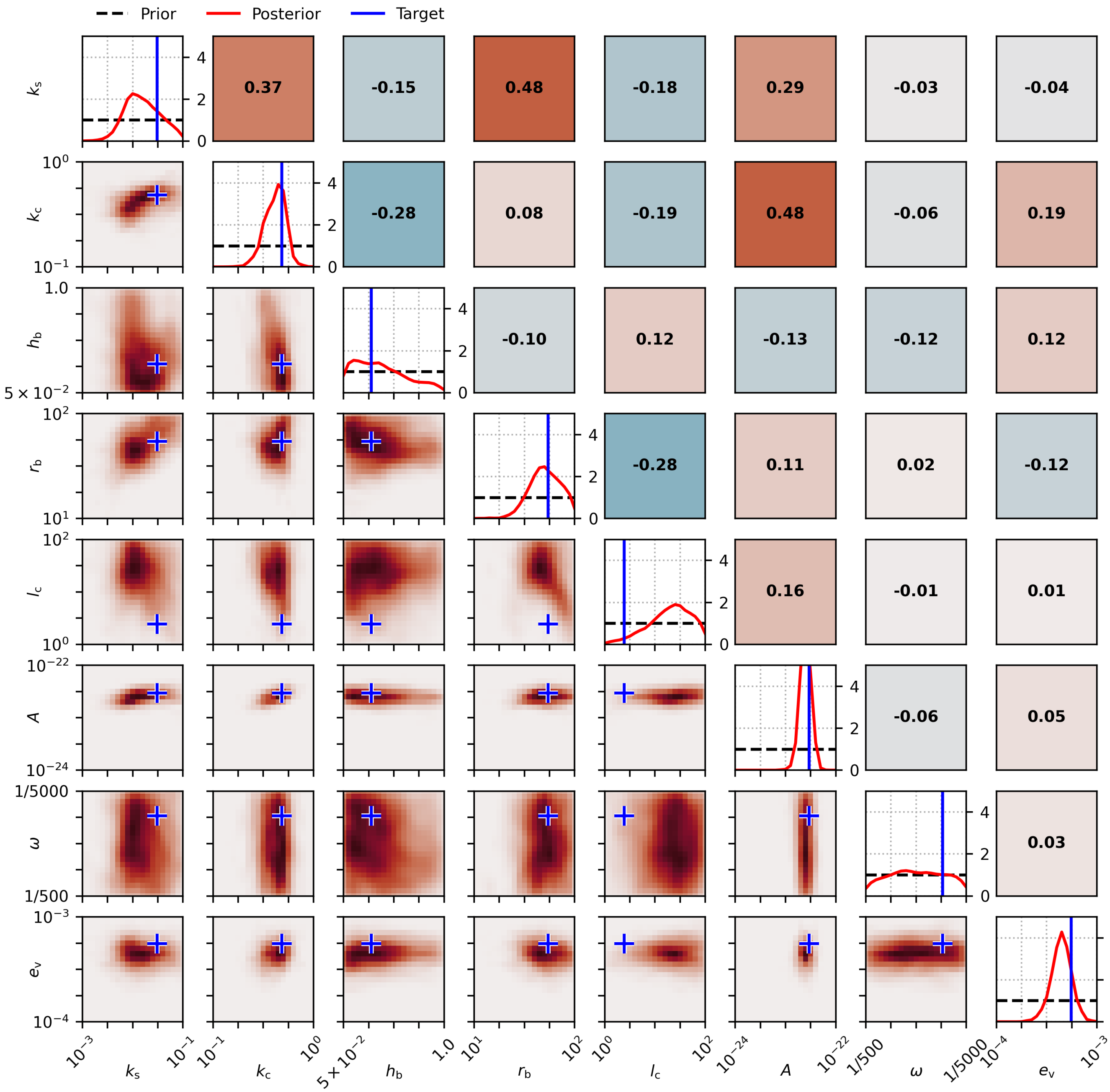

Fig. 4. Posterior distributions $P(\boldsymbol{\theta}|\boldsymbol{y})$ using synthetic water-pressure data. Diagonal panels show marginal prior and posterior distributions along with the hidden parameter values used to generate the synthetic data. Lower left panels show pairwise joint posterior distributions and values used to generate the data as crosses. Upper right panels show the estimated pairwise Pearson correlation coefficient.

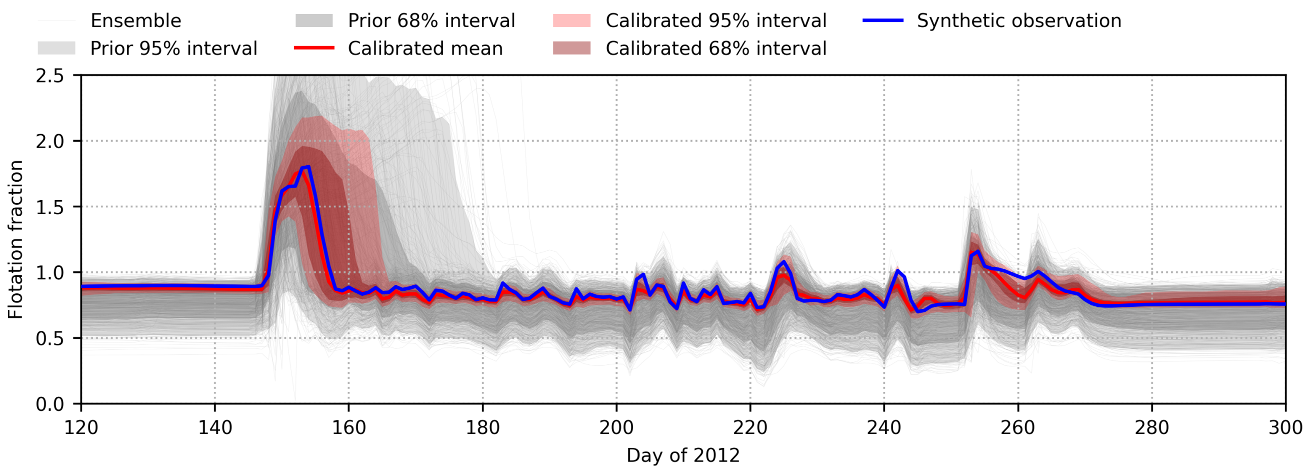

Fig. 5. Comparison of prior and calibrated ensembles of GlaDS simulations using the synthetic flotation-fraction timeseries. The mean and prediction intervals of the calibrated model are computed by running GlaDS with 256 samples from the posterior distribution.

5.3.1 Full timeseries calibration

As expected, calibration using the borehole water-pressure timeseries from 16 June to 31 December 2012 produces wider posterior distributions than the synthetic experiment (Fig. 6). Since we use the same prior distributions and GlaDS ensemble as in the synthetic experiment, these differences reflect how informative the real observations are compared to the synthetic observations. As we found in the synthetic calibration experiment, we obtain some constraint relative to the prior distribution on each parameter except the laminar–turbulent transition parameter ω. We obtain especially distinct posterior modes for channel conductivity $k_{\rm c}$, the bed bump aspect ratio $r_{\rm b}$ and the ice-flow coefficient A. The bed bump height $h_{\rm b}$, sheet-channel width $l_{\rm c}$ and englacial storage parameter $e_{\rm v}$ have indistinct modes but with a preference towards one side of their ranges. While we do resolve a posterior mode for the sheet conductivity $k_{\rm s}$, this peak is not consistently observed for all emulator architectures (i.e., p values, Fig. S9) or when using different subsets of the simulation ensemble (Fig. S10), so we do not consider this a robust estimate. There is moderate inverse correlation ($r = -0.43$) between the channel conductivity $k_{\rm c}$ and the sheet–channel width $l_{\rm c}$, with weaker correlations between other pairs. Compared to the synthetic experiment, even for parameters with a clear posterior mode (e.g., channel conductivity $k_{\rm c}$ and bed bump height $r_{\rm b}$), probability is nonzero across most of the range of values when using borehole data. The major exception is the ice-flow coefficient A, which has nearly zero marginal probability over most of its range except for the extreme upper end.

Calibrated model predictions (Fig. 7) highlight that, while the calibrated model sometimes aligns with the borehole timeseries, significant discrepancy remains between the calibrated model and the borehole timeseries. For instance, the coefficient of determination (the proportion of variance in the data explained by the calibrated model) is -3.2, where the negative indicates that the mean borehole flotation fraction is a better predictor than the calibrated model. For reference, the calibrated model predicts 93% of the variance in the synthetic calibration experiment. The negative coefficient of determination is a result of differences in the response to melt input variations between the calibrated model and the observations. The model consistently responds more strongly to increases in melt rate than the borehole water-pressure timeseries, rapidly increasing water pressure by 5% to >10% of overburden. For various instances, the borehole water-pressure timeseries shows negligible pressure variations (e.g., after day 250) or out-of-phase variations (e.g., near day 175) relative to the calibrated model. Following day ∼220, the observed baseline water pressure increases by ∼5% of overburden. This increase is not reproduced by the model for any parameter combinations, as evidenced by the intermittent lack of overlap of the model 95% prediction intervals with the observations. The borehole record unfortunately does not cover the spring speedup event associated with high modelled water pressures. The calibrated model, which is therefore relatively unconstrained in the spring, predicts unrealistically high water pressure from day ∼150–165, with the mean prediction exceeding 150% of overburden and the 95% prediction interval reaching nearly 250%.

5.3.2 Independent summer and winter calibration

A major shortcoming GlaDS and other similar models is that they typically produces low winter and high summer water pressures relative to measured or inferred water-pressure variations. This problem, in particular unrealistically high spring water pressure, persists in the calibrated model predictions. As one approach to improve the balance of winter and summer water pressure, Downs and others (2018) proposed using separate values for the sheet conductivity k_s within and outside of the melt season. To assess the extent to which we might infer distinct parameter values for these time periods, we separately calibrate the model using subsets of the borehole timeseries taken within and outside of the melt season. We use within melt season data between day 166 (the beginning of the record) until day 216, when the amplitude of diurnal variations suddenly decreases (not shown), suggesting the borehole may have lost full hydraulic connectivity. Since modelled and observed flotation fraction is nearly constant through winter, the principal

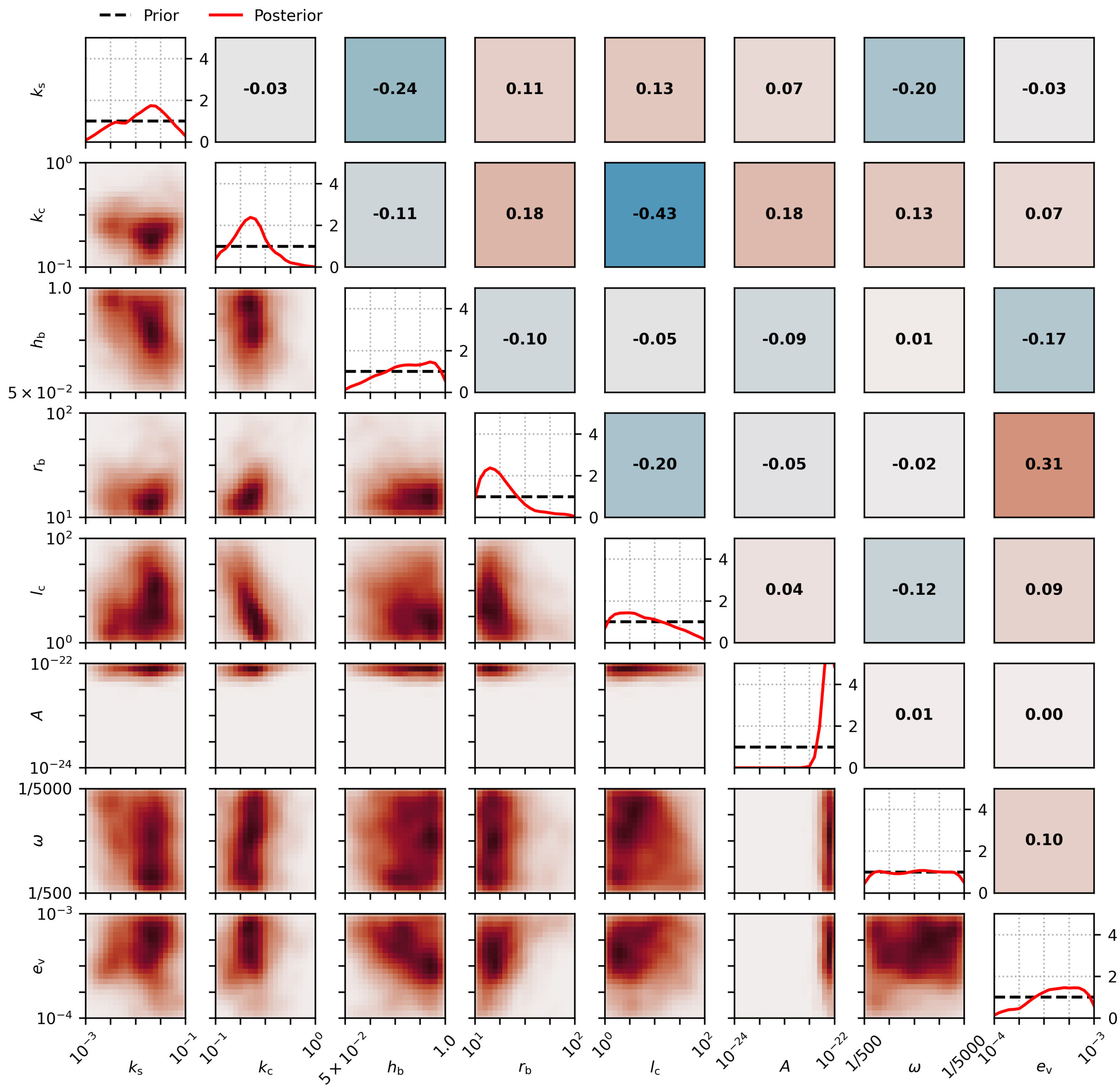

Fig. 6. Posterior distributions $P(\boldsymbol{\theta}|\boldsymbol{y})$ using borehole flotation-fraction data. Diagonal panels show marginal prior and posterior distributions. Lower left panels show pairwise joint posterior distributions. Upper right panels show the estimated pairwise Pearson correlation coefficient.

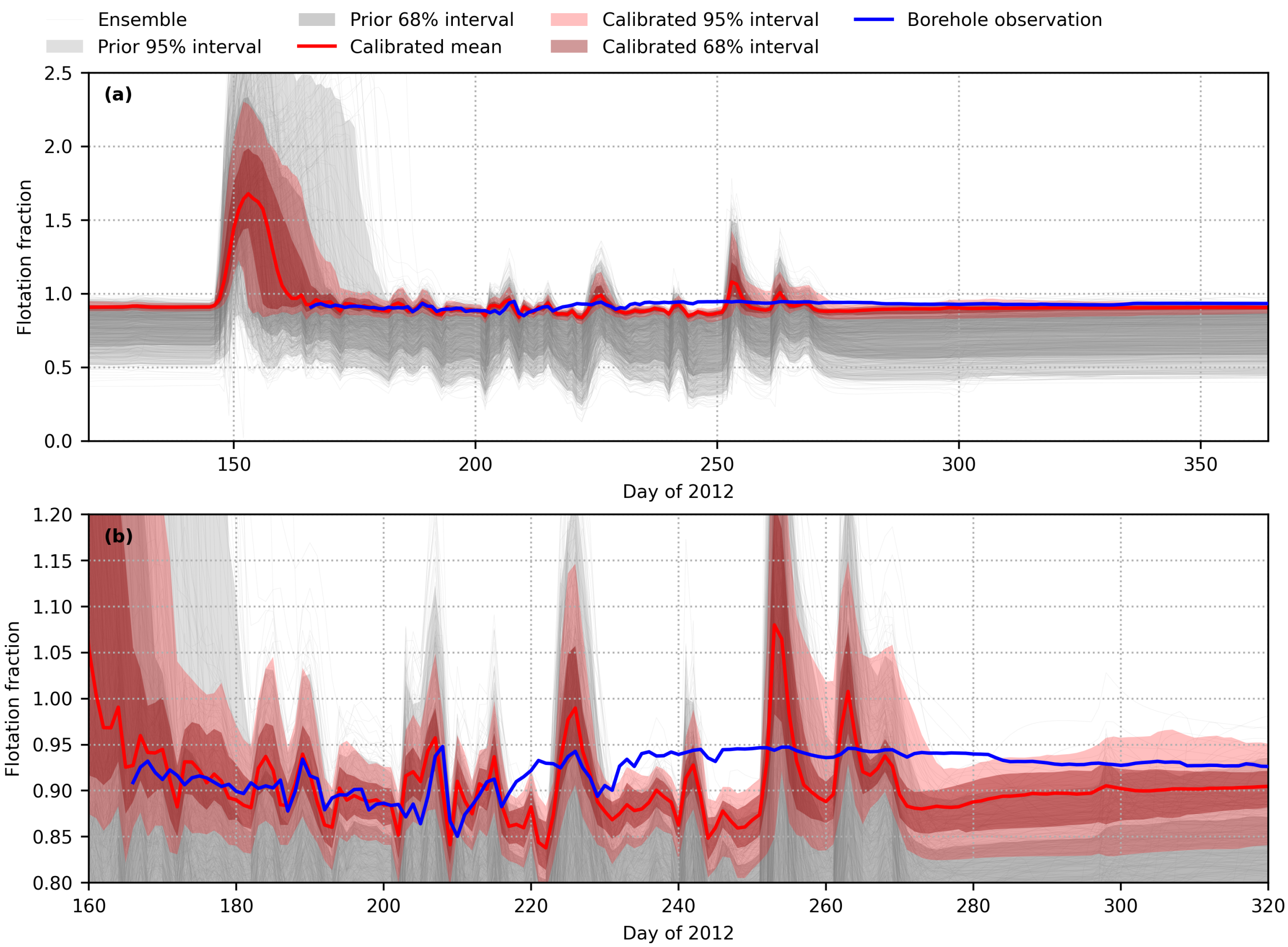

Fig. 7. Comparison of prior and calibrated ensembles of GlaDS simulations using the real borehole flotation-fraction timeseries. The mean and prediction intervals of the calibrated model are computed by running GlaDS with 256 samples from the posterior distribution.

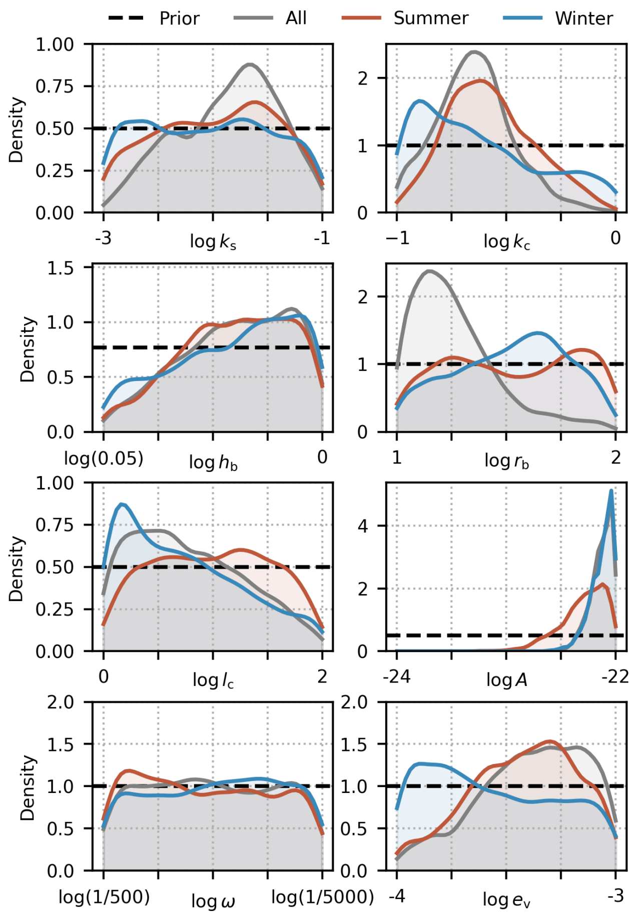

Fig. 8. Comparison of marginal posterior parameter distributions using all borehole data or separately using summer and winter data.

component decomposition does not add value in terms of describing flotation-fraction patterns (i.e., the first principal component explains $\gg$ 99% of the variance), and so we define the (scalar) winter flotation fraction as the average over the last 30 days of the year.

By using different subsets of the borehole timeseries, we infer distinct posterior modes with overlapping distributions for the channel conductivity k_c, bed bump aspect ratio r_b and englacial storage parameter e_v (Fig. 8). High values of the ice-flow coefficient A are preferred in all cases, but this preference is significantly weaker when using summer-only data. For the sheet conductivity k_s, the strongest posterior constraint is obtained by using the full timeseries. We do not find differences in the most-likely sheet conductivity values by separately using winter and summer data for calibration, despite the fact that the Downs and others (2018) sheet conductivity parameterization motivated this experiment. The distinct posterior parameter estimates for channel conductivity k_c and bed bump aspect ratio r_b act to increase winter water pressure and reduce summer pressure, consistent with the purpose but not the form of the sheet conductivity parameterization developed by Downs and others (2018). The englacial storage parameter e_v, which displays posterior modes at opposite extremes of its range using winter-only data compared to summer-only and all data, does not obviously fit this pattern. The preferentially high values using summer-only and all data may be a result of the model reducing the amplitude of the pressure response to surface melt events. While we have obtained some differences in estimated parameter values by using different subsets of the borehole data, we did not find a clear and useful pattern that supports seasonally changing GlaDS parameter values.

5.4 Posterior constraints on subglacial drainage system

In both synthetic and borehole experiments, the single point-scale timeseries reduces model uncertainty everywhere in the domain (Fig. 9). More uncertainty remains in the borehole calibration experiment, consistent with the wider spread in spring flotation-fraction predictions at the borehole location (Fig. 5, 7). In the synthetic calibration experiment, we have approximately halved the uncertainty in the total volume of the channel network relative to the spread of the original ensemble, with a posterior distribution consistent with the volume corresponding to the synthetic observation (Fig. 9d). In contrast, the borehole timeseries does not strongly constrain the volume of the channel network, but it does result in a preference towards larger channel networks than the original ensemble (Fig. 9e).

While the uncertainty in drainage system characteristics that remains after calibration with the borehole timeseries is larger than in the case of synthetic data, we do obtain meaningful constraints on channel network development throughout the domain and especially near the borehole location. Consistent with the channel network statistics (Fig. 9e), the model calibrated with the borehole timeseries shows, on average, higher channel discharge throughout the domain and especially within the Isunnguata Sermia sub-catchment (Fig. 10, see Fig. 1c for sub-catchment labels). Near the borehole, the calibrated model preferentially routes channelized flow along a consistent pathway that passes through the node used to represent the borehole. The calibrated model also has reduced flow through tributary branches which join below the borehole. Based on the difference in mean channel discharge, the borehole timeseries appears to provide some constraint on hydraulic potential gradients not only near the borehole but across the entire catchment.

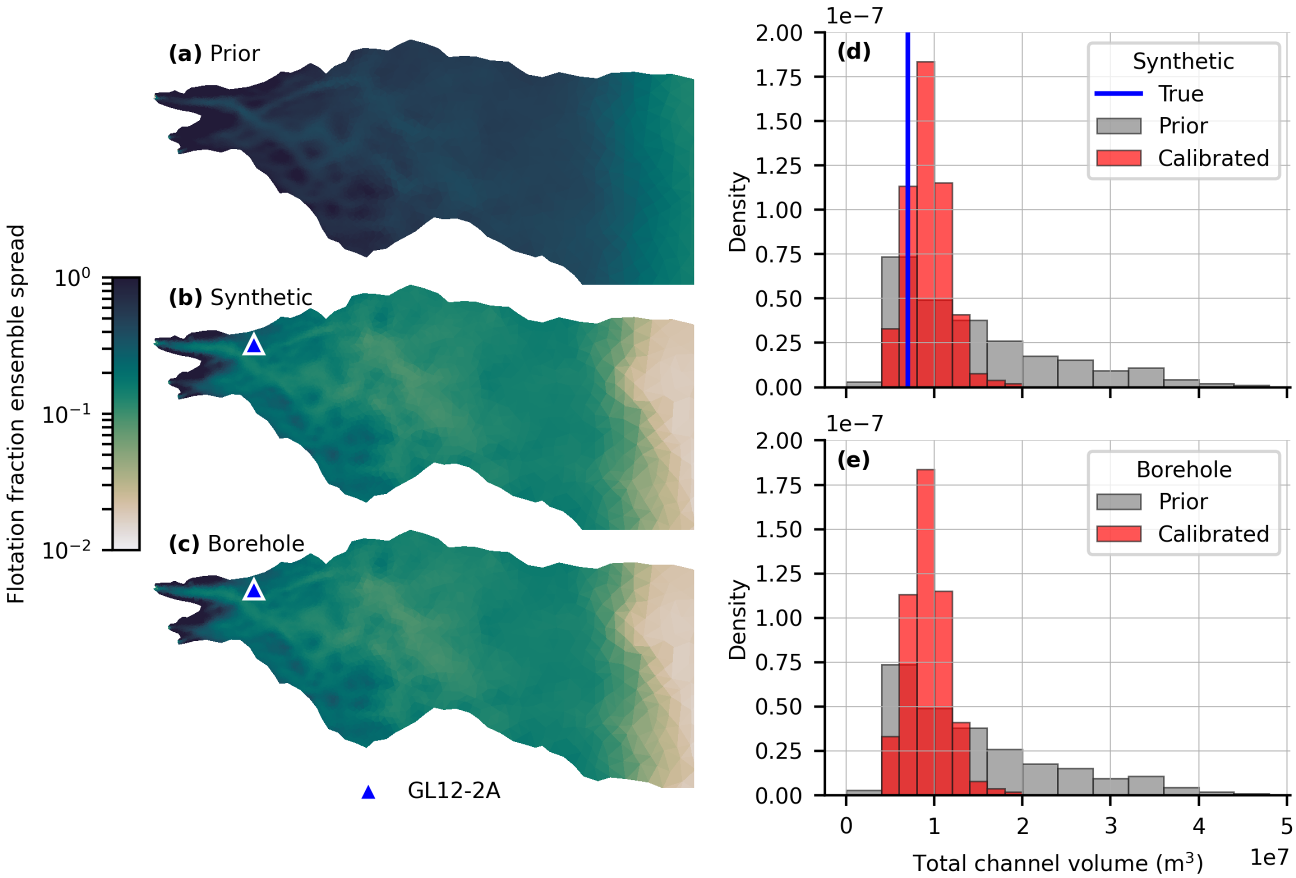

Fig. 9. Calibrated drainage system characteristics and uncertainty. (a–c) Melt season-averaged flotation-fraction ensemble spread as measured by the width of the 95% prediction intervals before calibration (a), after calibrating with synthetic observations (b) and after calibrating with borehole observations (c). (d–e) Prior and calibrated domain-integrated channel volume on day 229 (16 August) corresponding to synthetic (d) and borehole (e) observations. The true channel volume in (d) corresponds to the simulation used as synthetic observations.

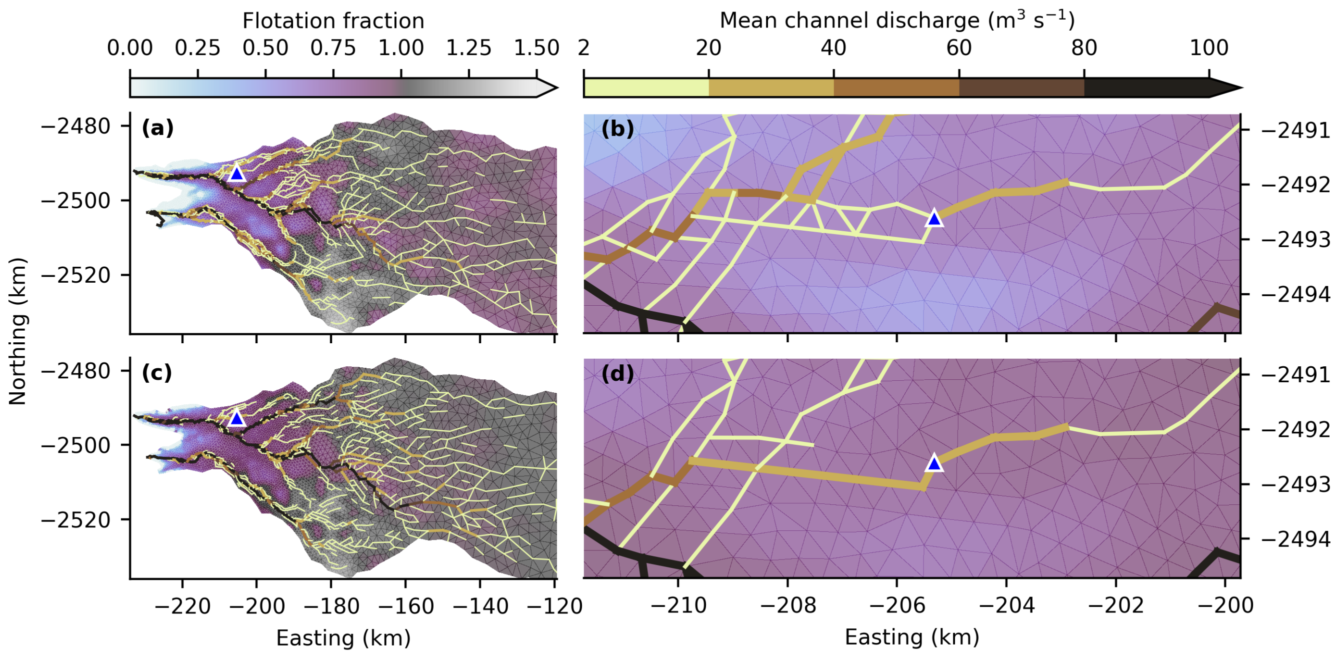

Fig. 10. Posterior channel network constraints. Mean channel discharge (using a minimum channel threshold $Q \geq 2\,\mathrm{m^3\,s^{-1}}$) on day 229 (16 August) for the area below 1850 m (left column) and near the borehole (right column) from the prior ensemble (top row) and after calibrating with borehole observations (bottom row). Mean flotation fraction for the corresponding ensembles is shown for context.

6 DISCUSSION

6.1 Parameter estimates

The synthetic calibration experiment shows that, even with perfect model–data fit, we do not learn about the true value of all parameters. This limitation arises in part because various parameter combinations produce similar outputs, as evidenced by the pairwise correlations up to $|r| \geq 0.4$), and also because the point-scale flotation fraction is not sensitive to all parameters (e.g., Hill and others, 2024a). The slight bias in the most-likely inferred values might be partially explained by differences between emulator predictions and GlaDS simulations, as evidenced by the reduction in bias associated with including more principal components (Fig. S9) and adding more GlaDS simulations (Fig. S10), both of which reduce emulator prediction error (Fig. S4).

The real borehole timeseries yields weaker parameter constraints than the synthetic experiment. This is to be expected given the shorter observation period, which does not include the spring event, and the serious model–data discrepancy (e.g., Fig. 7). Despite these limitations, the posterior parameter distributions can guide parameter selection to produce model outputs that are closer to reality than by using uncalibrated values. In the case of the ice-flow coefficient, the inferred value $A \approx 10^{-22}\,\mathrm{Pa}^{-3}\,\mathrm{s}^{-1}$ is outside the range typically suggested for basal ice at the pressure-melting point (e.g., Cuffey and Paterson, 2010) and perhaps points to model shortcomings and limitations in the model setup. However, it remains unclear what a reasonable upper bound on the ice-flow coefficient for cavity creep-closure should be given the anticipated high water content (e.g., macroscopic water content of 2.9–4.6% within temperate basal ice; Brown and others, 2017) and debris entrained within basal ice (e.g., Harper and others, 2017). Based on normal stress and sliding speed observations at Engabreen, Norway, Cohen (2000) inferred ice-flow coefficients for simple shear as high as $A = 1.5 \times 10^{-22}\,\mathrm{Pa}^{-3}\,\mathrm{s}^{-1}$. Cohen (2000) explains this high value, representing enhanced shear, as a consequence of bed-parallel unbound water layers laminated between layers of clean and dirty ice. Considering the influence of unknown, irregular cavity geometries on creep-closure rates (e.g., Helanow and others, 2021), it is not clear where to set a reasonable upper-bound for the creep-closure ice-flow coefficient.

Of the eight calibration parameters (Table 1), the sheet conductivity k_{s}, describing the transmissivity of the drainage system as a whole, the form of bed bumps as described by their height h_{b} and aspect ratio r_{b}, and the channel conductivity k_{c} most directly describe physical aspects of the subglacial drainage system. Other parameters are necessary for the model but describe aspects of the englacial drainage system (englacial storage parameter e_v) or basal ice that could be inferred through other means (ice-flow coefficient A), could be constrained by fluid-flow physics (laminar-turbulent transition parameter ω), or are model-specific parameters with little physical interpretation (sheet-width below channels l_c). The strongest constraints on physical subglacial hydraulic processes, therefore, would come from calibrating parameters in the first group listed above, however, we have obtained the strongest constraint on the ice-flow coefficient A. While the channel conductivity perhaps includes some information about subglacial and englacial conduits (e.g., Pohle and others, 2022), we do not robustly learn about the scale of cavities through the bed bump height h_b or the transmissivity of the drainage system through the sheet conductivity k_s (Fig. 6, S14). We have learned about the sheet conductivity in the synthetic calibration experiment, suggesting that model–data discrepancy, and perhaps the lack of borehole data during the spring, limits our ability to estimate this parameter from the data. In neither case do we learn about the bed bump height h_b, reinforcing that point-scale water pressure is not sensitive to h_b (e.g., Hill and others, 2024a).

The posterior estimates that we have derived based on calibration with the real borehole water-pressure timeseries differ from those derived by Brinkerhoff and others (2021) based on calibrating parameters of a coupled hydrology–ice-flow model applied to the same region in western Greenland. With a slightly modified version of GlaDS as the hydrology model, Brinkerhoff and others (2021) used a neural network emulator to estimate parameter distributions that produce the best fit to satellite-derived annual-average surface velocities. Our study and Brinkerhoff and others (2021) both constrain the most likely channel conductivity k_c, bed bump aspect ratio r_b, and to some extent, the englacial storage parameter e_v. We obtain overlapping estimates with Brinkerhoff and others (2021) for r_b and e_v, while our range of inferred k_c values is 2–3 orders of magnitude higher. In addition to the parameters that we are able to infer, Brinkerhoff and others (2021) constrain the value of the sheet conductivity k_s and the bed bump height h_b. We obtain a strong constraint on the ice-flow coefficient A, which Brinkerhoff and others (2021) did not calibrate. These studies infer different pairwise correlations between subglacial drainage model parameters. Brinkerhoff and others (2021) find correlation $r = -0.79$ between sheet conductivity k_s and the bed bump height h_b, while we find a much weaker relationship ($r = -0.24$). This difference may be a consequence of the different sheet-flow parameterizations and our inclusion of the ice-flow coefficient A as a calibration parameter. We find a correlation $r = 0.31$ between r_b and e_v, whereas Brinkerhoff and others (2021) report a slightly lower correlation of $r = 0.2$.

The comparable or stronger parameter constraints obtained by Brinkerhoff and others (2021) suggest that this single borehole water-pressure timeseries does not contain more information to constrain the parameters of subglacial drainage models than annual-average surface velocities, despite the impact of the filtering effect of ice flow on estimates based on surface velocities. This conclusion hinges on the discrepancy of the subglacial drainage model compared to the borehole water pressure since we obtain much more informative distributions when we remove the discrepancy by using synthetic model-generated data for calibration (Fig. 4). Moreover, Brinkerhoff and others (2021) do not consider the ice-flow coefficient A as a calibration parameter. Since we obtain the strongest constraint on A, it is possible that we would more strongly constrain other parameter values, particularly for parameters correlated with A, if we did not vary A across the ensemble. It is also possible that stronger constraints could be obtained with multiple, multi-year borehole water-pressure records that cover the full melt season including the spring speedup and a model that more closely matches the measured timeseries. With multiple multi-year borehole timeseries, it could also be worthwhile to repeat the separate summer–winter calibration experiment (Fig. 8) to reassess whether the results support seasonally varying parameter values (e.g., Downs and others, 2018). Combining both surface velocity observations and borehole water pressure data into a single calibration exercise could also provide stronger parameter estimates and further reduce prediction uncertainty.

6.2 Calibrated predictions and drainage-system characteristics

Using a single point-scale flotation-fraction timeseries, we have reduced the uncertainty in modelled flotation fraction and the configuration of subglacial channels by at least a factor of three in both synthetic and borehole experiments. Uncertainty reduction is appealing from a modelling perspective, however, it is concerning from the view of realistic subglacial drainage. Borehole records such as the one we have used to calibrate the model show pressure gradients as steep as $10\,\mathrm{kPa\,m^{-1}}$ between boreholes separated by tens of meters (e.g., Ryser and others, 2014; Wright and others, 2016) and hydraulic connectivity that varies over similar length scales (e.g., Wright and others, 2016; Rada Giacaman and Schoof, 2023). The lack of representation of this basal heterogeneity in models (c.f., Hoffman and others, 2016) results in unrealistically high confidence in inferred parameter values and calibrated predictions. The extent of overconfidence could be assessed by repeating the inference with multiple water-pressure timeseries from nearby boreholes that intersect hydraulically connected drainage, were such data available. For other model limitations, it is more challenging to assess how deficiencies in the theory underpinning models impacts uncertainty in the calibrated model (Section 6.5)

Table 3. Computation time corresponding to each step in the study. Computations were timed on AMD Rome 7532 CPUs on the Digital Research Alliance of Canada Narval cluster.

Task	CPU time (dd-HH:MM:ss)
Single GlaDS simulation	08:45:00
GlaDS ensemble	187-00:00:00
MCMC sampling	06:33:06 – 07:55:08
Likelihood evaluation	00:00:4.7 – 00:00:5.7
Emulator prediction	00:00:17
Calibrated GlaDS ensemble	93-00:00:00

6.3 Computational savings

The emulator accelerates MCMC sampling by $\sim$5000 times. This sampling density is not possible using GlaDS directly. Each GlaDS simulation takes $\sim$9 h, and since we have used 5000 MCMC samples, drawing this many MCMC samples would take $\sim$5 years since MCMC demands sequential evaluation. Using the GP emulator with 512 simulations and 12–15 PCs, drawing the MCMC samples takes $\sim$6.5-8 h. While more efficient sampling strategies are available that would require fewer samples, e.g., Metropolis-adjusted Langevin algorithm (Besag, 1994; Roberts and Tweedie, 1996) or No-U Turn Sampling (Hoffman and Gelman, 2014), emulator-based sampling will provide denser samples and more fully resolved posterior distributions than using GlaDS directly for any of these sampling strategies. While it seems that some of the bias in posterior modes (e.g., Fig. 4, S14, S15) may be partly a result of emulator error, this bias seems to be an appropriate trade-off for such a significant speedup in sampling.

6.4 Modelling limitations and challenges

We have made numerous choices in setting up the subglacial drainage model, for instance forbidding cavities from opening by viscous creep, using the laminar–turbulent sheet-flow model (Hill and others, 2024c), and using satellite-mapped moulin positions rather than transferring surface melt directly to the bed at each node. It would be possible to include the effect of these choices in the calibration by encoding them as categorical variables. We have instead opted to use the most physically justified option in each case and infer the corresponding parameter values conditioned on the model configuration.

For cavity creep opening, we argue that disallowing opening by viscous creep is the more physically realistic choice because of the disparate timescales between slow creep-opening (days to weeks) and the timescale corresponding to subglacial overpressurization (hours to days) along with the associated unmodelled processes (e.g., hydrofracture, Das and others, 2008; Tsai and Rice, 2010). Furthermore, allowing cavity creep-opening results in extensive regions (e.g., tens of kilometres inland along bed troughs) with sheet thicknesses exceeding the bed bump height for much of the melt season and effectively forming a subglacial lake. We have used the most realistic meltwater inputs reasonably possible at daily resolution, using moulins mapped from Landsat imagery (Yang and Smith, 2016) and surface runoff outputs from the RACMO2.3p2 model (Noël and others, 2018). The laminar–turbulent sheet-flow model is consistent with the well-understood physics of potential gradient-driven flow and produces improved winter water pressures relative to a turbulent-only model (Hill and others, 2024c).

Based on sensitivity tests, modelled water pressure at the borehole location is sensitive to the above modelling choices (Fig. S17). Despite efforts to produce a realistic, data-informed model setup, using a simpler, less realistic model results in a better fit to the borehole data in the case of cavity creep-opening and the moulin configuration (Fig. S18). For meltwater inputs through moulins, it is possible that we are missing additional moulins that are fed by streams that are too small to be resolved in the 15 m-resolution Landsat imagery (Yang and Smith, 2016). If this is the case, then a denser moulin configuration may result in model outputs closer to those obtained by transferring surface melt to the bed at every node, while being more realistic. The paradox that using more data in the model setup and intentionally choosing, *a priori*, the most reasonable parameterizations degrades model performance highlights the challenge of modelling subglacial drainage with the current generation of models and input data. It remains possible that two-way coupling with an ice-flow model which captures hydrology–sliding feedbacks could improve model outputs by reducing the amplitude of pressure variations and increasing winter water pressure (e.g., Hoffman and Price, 2014).

We have used daily average melt forcing and borehole water pressures, rather than resolving diurnal variations, to calibrate the drainage model because of the difficulty the model has in reproducing realistic diurnal variations and the challenge of constructing reasonably realistic sub-daily resolution melt inputs to drive the drainage model. When forced with diurnally varying melt inputs, GlaDS tends to produce muted variations over 24 h periods, with larger variations on multi-day timescales (e.g., Hill and others, 2024c). This incorrect spectral response is opposite to that shown by the borehole timeseries, which has variations in the baseline water pressure on the order of 5% of overburden, with diurnal variations up to 15% of overburden. Perhaps because the model does not produce strong diurnal variations, the model predicts minimal differences in drainage system evolution between daily and sub-daily forcing (Werder and others, 2013).

The discrepancy in spatial footprints of the observations and the model make it difficult to determine which node should be used as the most representative of the borehole observations. For the numerical mesh used here, there are three nodes similarly spaced within 386–454 m of the borehole (Fig. S1). We have chosen to use a node located in the centre of the trough that most consistently has a modelled subglacial channel passing through it (Fig. 10). Since water pressure sometimes varies between these three similarly distant nodes (Fig. S2), it would be best practice for future calibration studies to refine the model mesh around the location of any observations and consider forcing the mesh to have a node at the precise location of the borehole. Ideally, multiple borehole timeseries co-located within the same mesh element could be averaged to upscale the observations. However, the expense of drilling and the high likelihood of intersecting hydraulically isolated bed patches with any given borehole makes it rare to find multiple co-located boreholes suitable for comparison with continuum models.

6.5 Perspectives on subglacial drainage models

The discrepancy between the subglacial drainage model and reality (Fig. 7), and the finding that model predictions are made worse by including more physical insight when making model choices and using real data in the model configuration (Fig. S17, S18), suggests that we should ask: is the subglacial drainage model a useful representation of borehole water pressure? From the perspective of model–data misfit, the model is less useful than simply averaging the observations to obtain a single mean value of water pressure over time. In other words, the model does not effectively reproduce observed variations in borehole water pressure for any parameter values that we have tested. This conclusion does not even consider the behaviour of the model in the spring, when modelled pressure exceeds 150% of overburden for at least several days over a large portion of the domain, violating basic vertical force balance. It does not appear that the model–data misfit will improve with additional data to constrain it, since the misfit appears to be at least partially related to fundamental model shortcomings, rather than arising from residual parameter uncertainty which could plausibly be reduced by additional measurements.

Should the goal of subglacial drainage modelling be to precisely match individual borehole water-pressure timeseries? Borehole observations characteristically exhibit variability in baseline water pressure and the response to melt forcing over spatial scales of tens of meters or less (e.g., Murray and Clarke, 1995; Ryser and others, 2014; Wright and others, 2016). Considering that ice flow is sensitive to basal conditions averaged over scales of several ice thicknesses (e.g., Kamb and Echelmeyer, 1986), this does not seem like a productive goal for the purpose of explaining and predicting variations in sliding rates, which is the most common motivation for subglacial drainage model development. Instead, a more approachable goal would be to match the average features observed in multiple boreholes, intersecting both hydraulically isolated and connected drainage, within a spatial footprint of several ice-thicknesses.

These conclusion put modellers in a challenging position. It is well-understood that surface melt-forced variations in subglacial drainage influence glacier (e.g., Iken and Bindschadler, 1986) and ice-sheet dynamics (e.g., Joughin and others, 2008; Bartholomew and others, 2010; Palmer and others, 2011). However, our application of a popular subglacial drainage model suggests that it cannot reasonably reproduce direct measurements of subglacial drainage, even when calibrated with real data and parametric uncertainties are accounted for. We suggest that a productive path forward is to re-examine the overall structure of subglacial hydrology models, for instance englacial storage, processes associated with pressures exceeding overburden (e.g., Tsai and Rice, 2010; Schoof and others, 2012), two-way hydrology–sliding feedbacks (e.g., Hoffman and Price, 2014), the form of the relationship between hydrology and basal friction (e.g., Gilbert and others, 2022) and heterogeneous hydraulic connectivity (Hoffman and others, 2016), to improve model behaviour on appropriate spatial and temporal scales. Concurrently, ice-flow models could adopt effective-pressure parameterizations that are consistent with observed borehole water pressures, e.g., effective pressure $N =$ 5–20% of overburden (e.g., Wright and others, 2016) until such subglacial drainage models are developed.

7 CONCLUSIONS

We have applied an emulator-based Bayesian calibration method to enable efficient Bayesian inference of parameters of the GlaDS subglacial hydrology model (Werder and others, 2013) given timeseries observations of flotation fraction (i.e., water pressure relative to ice overburden) at daily resolution. Using borehole water-pressure data from western Greenland, we obtain meaningful constraints on the channel conductivity k_{c}, bed bump height r_{b}, ice-flow coefficient A and englacial storage parameter e_{v}, with correspondingly reduced uncertainty in modelled water pressure. Relative to the uncalibrated model, we have constrained the configuration of subglacial channels near the borehole and, to a lesser degree, across the entire catchment.

The calibrated water-pressure timeseries overlaps with the overall range of water pressure observed in the borehole, but the calibrated predictions fail to match observed surface melt-forced water-pressure variations. We have shown that this discrepancy between modelled subglacial drainage and borehole observations is not a result of the choice of model parameters, but is rather a structural feature of the model and therefore is unlikely to be reduced by integrating additional field data. While it is unreasonable to expect a spatially distributed continuum model to precisely predict point-scale (i.e., borehole) water-pressure variations, the structural discrepancy suggests that the limitations of physics-based drainage models, rather than parameter uncertainty or their computational cost, are a rate-limiting step in predicting hydraulically-forced seasonal ice-flow variations.

CODE AND DATA AVAILABILITY

Code for running experiments and calibrating the drainage model is available at `https://github.com/timghill/glads-borehole-calibration/` (Hill and others, 2024b). Model inputs, outputs and trained models will be made available before publication. The SEPIA package v1.1 (Gattiker and others, 2020), used for emulator-based Bayesian inference, is available at `https://github.com/lanl/SEPIA/`. The Ice-sheet and Sea-level System Model (ISSM) used for GlaDS simulations is available at `https://issm.jpl.nasa.gov/` (Larour and others, 2012). Daily surface runoff outputs from the 5.5 km-resolution RACMO2.3p2 model are available by contacting the Institute for Marine and Atmospheric research Utrecht.

ACKNOWLEDGEMENTS

TH was supported by Simon Fraser University and the Natural Sciences and Engineering Research Council of Canada (NSERC) Canada Graduate Scholarship program. GF received support from the NSERC Discovery Grants program. Support for MH was provided through the Scientific Discovery through Advanced Computing (SciDAC) program funded by the U.S. Department of Energy (DOE), Office of Science, Advanced Scientific Computing Research and Biological and Environmental Research Programs. This research was enabled in part by support provided by WestDRI (`https://training.westdri.ca`), Calcul Quebec (`https://www.calculquebec.ca/`) and the Digital Research Alliance of Canada (`https://alliancecan.ca`). RACMO2.3p2 model outputs were kindly provided by Christiaan van Dalum. We would also like to thank Joel Harper for helpful discussions and for providing borehole data.

AUTHOR CONTRIBUTIONS

GF, TH and MH conceived of the idea of constraining subglacial drainage model parameters with water-pressure timeseries. TH and DB contributed to the emulator and calibration methodology with input from MH. TH, GF, and MH constructed the subglacial drainage model setup. TH developed and ran the code and visualized the outputs. TH led the manuscript preparation with contributions from GF, DB and MH. All authors interpreted the calibration results and edited the manuscript.

REFERENCES

Andrews LC, Catania GA, Hoffman MJ, Gulley JD, Lüthi MP, Ryser C, Hawley RL and Neumann TA (2014) Direct observations of evolving subglacial drainage beneath the Greenland ice sheet. *Nature*, **514**(7520), 80–83 (doi: 10.1038/nature13796)

Bartholomew I, Nienow P, Mair D, Hubbard A, King M and Sole A (2010) Seasonal evolution of subglacial drainage and acceleration in a Greenland outlet glacier. *Nature Geoscience*, **3**, 408–4011 (doi: 10.1038/ngeo863)

Bartholomew I, Nienow P, Sole A, Mair D, Cowton T, Palmer S and Wadham J (2011) Supraglacial forcing of subglacial drainage in the ablation zone of the Greenland ice sheet. *Geophysical Research Letters*, **38**(8) (doi: 10.1029/2011GL047063)

Besag J (1994) Discussion of the Paper by Grenander and Miller. *Journal of the Royal Statistical Society: Series B (Methodological)*, **56**(4), 591–592, ISSN 0035-9246 (doi: 10.1111/j.2517-6161.1994.tb02001.x)

Brinkerhoff D, Aschwanden A and Fahnestock M (2021) Constraining subglacial processes from surface velocity observations using surrogate-based Bayesian inference. *Journal of Glaciology*, **67**(263), 385–403

Brown J, Harper J and Humphrey N (2017) Liquid water content in ice estimated through a full-depth ground radar profile and borehole measurements in western Greenland. *The Cryosphere*, **11**(1), 669–679 (doi: 10.5194/tc-11-669-2017)

Cohen D (2000) Rheology of ice at the bed of Engabreen, Norway. *Journal of Glaciology*, **46**(155), 611–621 (doi: 10.3189/172756500781832620)

Cook SJ, Christoffersen P, Todd J, Slater D and Chauché N (2020) Coupled modelling of subglacial hydrology and calving-front melting at Store Glacier, West Greenland. *The Cryosphere*, **14**(3), 905–924 (doi: 10.5194/tc-14-905-2020)

Cuffey KM and Paterson WSB (2010) *The physics of glaciers*. Academic Press, ISBN 9780080919126

Das SB, Joughin I, Behn MD, Howat IM, King MA, Lizarralde D and Bhatia MP (2008) Fracture propagation to the base of the Greenland ice sheet during supraglacial lake drainage. *Science*, **320**(5877), 778–781 (doi: 10.1126/science.1153360)

Derkacheva A, Gillet-Chaulet F, Mouginot J, Jager E, Maier N and Cook S (2021) Seasonal evolution of basal environment conditions of Russell sector, West Greenland, inverted from satellite observation of surface flow. *The Cryosphere*, **15**(12), 5675–5704 (doi: 10.5194/tc-15-5675-2021)

Dow C, McCormack F, Young D, Greenbaum J, Roberts J and Blankenship D (2020) Totten Glacier subglacial hydrology determined from geophysics and modeling. *Earth and Planetary Science Letters*, **531**, 115961, ISSN 0012-821X (doi: 10.1016/j.epsl.2019.115961)

Dow CF (2022) The role of subglacial hydrology in Antarctic ice sheet dynamics and stability: a modelling perspective. *Annals of Glaciology*, **63**(87–89), 49–54 (doi: 10.1017/aog.2023.9)

Downs J, Brinkerhoff D and Morlighem M (2023) Inferring time-dependent calving dynamics at Helheim Glacier. *Journal of Glaciology*, **69**(274), 381–396 (doi: 10.1017/jog.2022.68)

Downs JZ, Johnson JV, Harper JT, Meierbachtol T and Werder MA (2018) Dynamic hydraulic conductivity reconciles mismatch between modeled and observed winter subglacial water pressure. *Journal of Geophysical Research: Earth Surface*, **123**(4), 818–836 (doi: 10.1002/2017JF004522)

Ehrenfeucht S, Morlighem M, Rignot E, Dow CF and Mouginot J (2023) Seasonal acceleration of Petermann Glacier, Greenland, from changes in subglacial hydrology. *Geophysical Research Letters*, **50**(1), e2022GL098009 (doi: 10.1029/2022GL098009)

Gagliardini O and Werder MA (2018) Influence of increasing surface melt over decadal timescales on land-terminating Greenland-type outlet glaciers. *Journal of Glaciology*, **64**(247), 700–710 (doi: 10.1017/jog.2018.59)

Gattiker J, Klein N, Hutchings G and Lawrence E (2020) lanl/SEPIA: v1.1 [Software]. *Zenodo* (doi: 10.5281/zenodo.4048801)

Gelman A, Carlin J, Stern H, Dunson D, Vehtari A and Rubin D (2013) *Bayesian data analysis*. Chapman and Hall/CRC, New York, 3rd edition

Gilbert A, Gimbert F, Thøgersen K, Schuler TV and Kääb A (2022) A consistent framework for coupling basal friction with subglacial hydrology on hard-bedded glaciers. *Geophysical Research Letters*, **49**(13), e2021GL097507 (doi: 10.1029/2021GL097507)

Hager AO, Hoffman MJ, Price SF and Schroeder DM (2022) Persistent, extensive channelized drainage modeled beneath Thwaites Glacier, West Antarctica. *The Cryosphere*, **16**(9), 3575–3599 (doi: 10.5194/tc-16-3575-2022)

Harper J, Meierbachtol T, Humphrey N, Saito J and Stansberry A (2021) Generation and fate of basal meltwater during winter, western Greenland ice sheet. *The Cryosphere*, **15**(12), 5409–5421 (doi: 10.5194/tc-15-5409-2021)

Harper JT, Humphrey NF, Meierbachtol TW, Graly JA and Fischer UH (2017) Borehole measurements indicate hard bed conditions, Kangerlussuaq sector, western Greenland ice sheet. *Journal of Geophysical Research: Earth Surface*, **122**(9), 1605–1618 (doi: 10.1002/2017JF004201)

Helanow C, Iverson NR, Woodard JB and Zoet LK (2021) A slip law for hard-bedded glaciers derived from observed bed topography. *Science Advances*, **7**(20), eabe7798 (doi: 10.1126/sciadv.abe7798)

Hepburn AJ, Dow CF, Ojala A, Mäkinen J, Ahokangas E, Hovikoski J, Palmu JP and Kajuutti K (2024) The organization of subglacial drainage during the demise of the Finnish Lake District Ice Lobe. *The Cryosphere*, **18**(10), 4873–4916 (doi: 10.5194/tc-18-4873-2024)

Higdon D, Kennedy M, Cavendish JC, Cafeo JA and Ryne RD (2004) Combining field data and computer simulations for calibration and prediction. *SIAM Journal on Scientific Computing*, **26**(2), 448–466 (doi: 10.1137/S1064827503426693)

Higdon D, Gattiker J, Williams B and Rightley M (2008) Computer model calibration using high-dimensional output. *Journal of the American Statistical Association*, **103**(482), 570–583 (doi: 10.1198/016214507000000888)

Hill T, Bingham D, Flowers GE and Hoffman MJ (2024a) Computationally efficient subglacial drainage modeling with gaussian process emulation: GlaDS-GP v1.0. *ESS Open Archive Preprint* (doi: 10.22541/essoar.172736254.41350153/v2)

Hill T, Flowers GE, Bingham D and Hoffman MJ (2024b) timghill/glads-borehole-calibration: v1.0.0 [Software]. *Github*, https://github.com/timghill/glads-borehole-calibration

Hill T, Flowers GE, Hoffman MJ, Bingham D and Werder MA (2024c) Improved representation of laminar and turbulent sheet flow in subglacial drainage models. *Journal of Glaciology*, **70**, e24 (doi: 10.1017/jog.2023.103)

Hoffman MD and Gelman A (2014) The No-U-Turn Sampler: Adaptively setting path lengths in Hamiltonian Monte Carlo. *Jornal of Machine Learning Research*, **15**(1), 1593 – 1623

Hoffman MJ and Price S (2014) Feedbacks between coupled subglacial hydrology and glacier dynamics. *Journal of Geophysical Research: Earth Surface*, **119**(3), 414–436 (doi: 10.1002/2013JF002943)

Hoffman MJ, Andrews LC, Price SF, Catania GA, Neumann TA, Lüthi MP, Gulley J, Ryser C, Hawley RL and Morriss B (2016) Greenland subglacial drainage evolution regulated by weakly connected regions of the bed. *Nature communications*, **7**(1), 13903 (doi: 10.1038/ncomms13903)

Iken A and Bindschadler RA (1986) Combined measurements of subglacial water pressure and surface velocity of Findelengletscher, Switzerland: Conclusions about drainage system and sliding mechanism. *Journal of Glaciology*, **32**(110), 101–119 (doi: 10.3189/S0022143000006936)

Irarrazaval I, Werder MA, Linde N, Irving J, Herman F and Mariethoz G (2019) Bayesian inference of subglacial channel structures from water pressure and tracer-transit time data: A numerical study based on a 2-D geostatistical modeling approach. *Journal of Geophysical Research: Earth Surface*, **124**(6), 1625–1644 (doi: 10.1029/2018JF004921)

Irarrazaval I, Werder MA, Huss M, Herman F and Mariethoz G (2021) Determining the evolution of an alpine glacier drainage system by solving inverse problems. *Journal of Glaciology*, **67**(263), 421–434 (doi: 10.1017/jog.2020.116)

Joughin I, Das SB, King MA, Smith BE, Howat IM and Moon T (2008) Seasonal speedup along the western flank of the Greenland ice sheet. *Science*, **320**(5877), 781–783 (doi: 10.1126/science.1153288)

Joughin I, Smith B, Howat I and Scambos T (2016) MEaSUREs Multi-year Greenland Ice Sheet Velocity Mosaic, Version 1 (doi: 10.5067/QUA5Q9SVMSJG), Date Accessed 2024-06-10

Joughin I, Smith BE and Howat IM (2018) A complete map of Greenland ice velocity derived from satellite data collected over 20 years. *Journal of Glaciology*, **64**(243), 1–11 (doi: 10.1017/jog.2017.73)

Kamb B and Echelmeyer KA (1986) Stress-gradient coupling in glacier flow: I. Longitudinal averaging of the influence of ice thickness and surface slope. *Journal of Glaciology*, **32**(111), 267–284 (doi: 10.3189/S0022143000015604)

Kennedy MC and O'Hagan A (2001) Bayesian calibration of computer models. *Journal of the Royal Statistical Society: Series B (Statistical Methodology)*, **63**(3), 425–464 (doi: 10.1111/1467-9868.00294)

Khan SA, Morlighem M, Ehrenfeucht S, Seroussi H, Choi Y, Rignot E, Humbert A, Pickell D and Hassan J (2024) Inland summer speedup at Zachariæ Isstrøm, northeast Greenland, driven by subglacial hydrology. *Geophysical Research Letters*, **51**(18), e2024GL110691 (doi: 10.1029/2024GL110691)

Larour E, Seroussi H, Morlighem M and Rignot E (2012) Continental scale, high order, high spatial resolution, ice sheet modeling using the Ice Sheet System Model (ISSM). *Journal of Geophysical Research: Earth Surface*, **117**, F01022 (doi: 10.1029/2011JF002140)

Lindbäck K, Pettersson R, Hubbard AL, Doyle SH, van As D, Mikkelsen AB and Fitzpatrick AA (2015) Subglacial water drainage, storage, and piracy beneath the Greenland ice sheet. *Geophysical Research Letters*, **42**(18), 7606–7614 (doi: 10.1002/2015GL065393)

Meierbachtol T, Harper J and Humphrey N (2013) Basal drainage system response to increasing surface melt on the Greenland ice sheet. *Science*, **341**(6147), 777–779 (doi: 10.1126/science.1235905)

Meierbachtol TW, Harper JT, Johnson JV, Humphrey NF and Brinkerhoff DJ (2015) Thermal boundary conditions on western Greenland: Observational constraints and impacts on the modeled thermomechanical state. *Journal of Geophysical Research: Earth Surface*, **120**(3), 623–636 (doi: 10.1002/2014JF003375)

Meierbachtol TW, Harper JT, Humphrey NF and Wright PJ (2016) Mechanical forcing of water pressure in a hydraulically isolated reach beneath Western Greenland's ablation zone. *Annals of Glaciology*, **57**(72), 62–70 (doi: 10.1017/aog.2016.5)

Morlighem M and others (2022) IceBridge BedMachine Greenland, Version 5 [Dataset] (doi: 10.5067/GMEVBWFLWA7X), Date Accessed 2024-05-16

Morlighem M, Williams CN, Rignot E, An L, Arndt JE, Bamber JL, Catania G, Chauché N, Dowdeswell JA, Dorschel B, Fenty I, Hogan K, Howat I, Hubbard A, Jakobsson M, Jordan TM, Kjeldsen KK, Millan R, Mayer L, Mouginot J, Noël BPY, O'Cofaigh C, Palmer S, Rysgaard S, Seroussi H, Siegert MJ, Slabon P, Straneo F, van den Broeke MR, Weinrebe W, Wood M and Zinglersen KB (2017) BedMachine v3: Complete bed topography and ocean bathymetry mapping of Greenland from multibeam echo sounding combined with mass conservation. *Geophysical Research Letters*, **44**(21), 11,051–11,061 (doi: 10.1002/2017GL074954)

Murray T and Clarke GKC (1995) Black-box modeling of the subglacial water system. *Journal of Geophysical Research: Solid Earth*, **100**(B6), 10231–10245 (doi: 10.1029/95JB00671)

Nanni U, Gimbert F, Roux P and Lecointre A (2021) Observing the subglacial hydrology network and its dynamics with a dense seismic array. *Proceedings of the National Academy of Sciences*, **118**(28), e2023757118 (doi: 10.1073/pnas.2023757118)

Noël B, van de Berg WJ, van Wessem JM, van Meijgaard E, van As D, Lenaerts JTM, Lhermitte S, Kuipers Munneke P, Smeets CJPP, van Ulft LH, van de Wal RSW and van den Broeke MR (2018) Modelling the climate and surface mass balance of polar ice sheets using RACMO2 – Part 1: Greenland (1958–2016). *The Cryosphere*, **12**(3), 811–831 (doi: 10.5194/tc-12-811-2018)

Palmer S, Shepherd A, Nienow P and Joughin I (2011) Seasonal speedup of the Greenland Ice Sheet linked to routing of surface water. *Earth and Planetary Science Letters*, **302**(3), 423–428 (doi: 10.1016/j.epsl.2010.12.037)

Pohle A, Werder MA, Gräff D and Farinotti D (2022) Characterising englacial R-channels using artificial moulins. *Journal of Glaciology*, **68**(271), 879–890 (doi: 10.1017/jog.2022.4)

Rada Giacaman CA and Schoof C (2023) Channelized, distributed, and disconnected: spatial structure and temporal evolution of the subglacial drainage under a valley glacier in the Yukon. *The Cryosphere*, **17**(2), 761–787 (doi: 10.5194/tc-17-761-2023)

Roberts GO and Tweedie RL (1996) Exponential convergence of Langevin distributions and their discrete approximations. *Bernoulli*, **2**(4), 341 – 363

Ryser C, Lüthi MP, Andrews LC, Catania GA, Funk M, Hawley R, Hoffman M and Neumann TA (2014) Caterpillar-like ice motion in the ablation zone of the Greenland ice sheet. *Journal of Geophysical Research: Earth Surface*, **119**(10), 2258–2271 (doi: 10.1002/2013JF003067)

Schoof C, Hewitt IJ and Werder MA (2012) Flotation and free surface flow in a model for subglacial drainage. Part 1. Distributed drainage. *Journal of Fluid Mechanics*, **702**, 126–156 (doi: 10.1017/jfm.2012.165)

Smeets PC, Kuipers Munneke P, Van As D, van den Broeke MR, Boot W, Oerlemans H, Snellen H, Reijmer CH and van de Wal RS (2018) The K-transect in west Greenland: Automatic weather station data (1993–2016). *Arctic, Antarctic, and Alpine Research*, **50**(1), S100002 (doi: 10.1080/15230430.2017.1420954)

Sobol' IM (1967) On the distribution of points in a cube and the approximate evaluation of integrals. *Zhurnal Vychislitel'noi Matematiki i Matematicheskoi Fiziki*, **7**(4), 784–802

Sole A, Nienow P, Bartholomew I, Mair D, Cowton T, Tedstone A and King MA (2013) Winter motion mediates dynamic response of the Greenland ice sheet to warmer summers. *Geophysical Research Letters*, **40**(15), 3940–3944 (doi: 10.1002/grl.50764)

Sommers AN, Meyer CR, Poinar K, Mejia J, Morlighem M, Rajaram H, Warburton KLP and Chu W (2024) Velocity of Greenland's Helheim glacier controlled both by terminus effects and subglacial hydrology with distinct realms of influence. *Geophysical Research Letters*, **51**(15), e2024GL109168 (doi: 10.1029/2024GL109168)

Tsai VC and Rice JR (2010) A model for turbulent hydraulic fracture and application to crack propagation at glacier beds. *Journal of Geophysical Research: Earth Surface*, **115**, F03007 (doi: 10.1029/2009JF001474)

van de Wal RSW, Boot W, van den Broeke MR, Smeets CJPP, Reijmer CH, Donker JJA and Oerlemans J (2008) Large and rapid melt-induced velocity changes in the ablation zone of the Greenland ice sheet. *Science*, **321**(5885), 111–113 (doi: 10.1126/science.1158540)

Verjans V and Robel A (2024) Accelerating subglacial hydrology for ice sheet models with deep learning methods. *Geophysical Research Letters*, **51**(2), e2023GL105281 (doi: 10.1029/2023GL105281)

Wearing MG, Dow CF, Goldberg DN, Gourmelen N, Hogg AE and Jakob L (2024) Characterizing subglacial hydrology within the Amery Ice Shelf catchment using numerical modeling and satellite altimetry. *Journal of Geophysical Research: Earth Surface*, **129**(4), e2023JF007421 (doi: 10.1029/2023JF007421)

Werder MA and Funk M (2009) Dye tracing a jökulhlaup: II. testing a jökulhlaup model against flow speeds inferred from measurements. *Journal of Glaciology*, **55**(193), 899–908 (doi: 10.3189/002214309790152375)

Werder MA, Hewitt IJ, Schoof CG and Flowers GE (2013) Modeling channelized and distributed subglacial drainage in two dimensions. *Journal of Geophysical Research: Earth Surface*, **118**(4), 2140–2158 (doi: 10.1002/jgrf.20146)

Wright PJ, Harper JT, Humphrey NF and Meierbachtol TW (2016) Measured basal water pressure variability of the western Greenland ice sheet: Implications for hydraulic potential. *Journal of Geophysical Research: Earth Surface*, **121**(6), 1134–1147 (doi: 10.1002/2016JF003819)

Yang K and Smith LC (2016) Internally drained catchments dominate supraglacial hydrology of the southwest Greenland ice sheet. *Journal of Geophysical Research: Earth Surface*, **121**(10), 1891–1910 (doi: 10.1002/2016JF003927)